Journal of Radiology and Imaging

NobleResearch
An Open Access Publisher
www.nobleresearch.org

Iwasaki A et al., J Radiol Imaging. 2017, 2(3):14-35
http://dx.doi.org/10.14312/2399-8172.2017-4

Original research

Open Access

10-MV X-ray dose calculation in water for MLC and wedge fields using a convolution method with X-ray spectra reconstructed as a function of off-axis distance

Akira Iwasaki[1,*], Shigenobu Kimura[2], Kohji Sutoh[2], Kazuo Kamimura[2], Makoto Sasamori[3], Morio Seino[4], Fumio Komai[4], Masafumi Takagi[5], Shingo Terashima[6], Yoichiro Hosokawa[6], Hidetoshi Saitoh[7] and Masanori Miyazawa[8]

[1] 2-3-24 Shimizu, Hirosaki, Aomori 036-8254, Japan
[2] Department of Radiology, Aomori City Hospital, 1-14-20 Katta, Aomori 030-0821, Japan
[3] Department of Radiology, Misawa City Hospital, 4-1-10 Chuo-cho, Misawa, Aomori 033-0051, Japan
[4] Department of Radiology, Hirosaki University Hospital, 53 Hon-cho, Hirosaki, Aomori 036-8563, Japan
[5] Department of Radiology, Hirosaki Chuo Hospital, 3-1 Yoshino-cho, Hirosaki, Aomori 036-8188, Japan
[6] Graduate School of Health Sciences, Hirosaki University, 66-1 Hon-cho, Hirosaki, Aomori 036-8564, Japan
[7] Graduate School of Human Health Sciences, Tokyo Metropolitan University, 7-2-10 Higashi-Ogu, Arakawa-ku, Tokyo, 116-8551, Japan
[8] Technology of Radiotherapy Corporation, 2-1-2 Koishikawa, Bunkyo-ku, Tokyo, 175-0092, Japan

Abstract

Purposes: This paper highlights a 10-MV X-ray convolution dose calculation method in water using primary and scatter dose kernels formed for energy bins of X-ray spectra reconstructed as a function of the off-axis distance for a linear accelerator equipped with pairs of upper and lower jaws, a multileaf collimator (MLC) and a wedge filter. *Methods:* The reconstructed X-ray spectra set was composed of 11 energy bins. To estimate the in-air beam intensities at points on the isocenter plane for an MLC field, we employed an MLC leaf-field output subtraction method, using an extended radiation source on each of the X-ray target and the flattening filter as well as simplified two-dimensional plates to simulate the three-dimensional jaws and MLC structures. A special correction factor was introduced for nonuniform incident beam intensities, particularly produced at MLC fields. The in-phantom dose calculation was performed by treating the phantom, the wedge filter, the wedge holder and the MLC as parts of a unified irradiated body, where we proposed to use a special factor for the density scaling theorem within the unified irradiated body. *Conclusions:* The phantom dose was generally separated into nine dose-components: the primary and scatter dose-components produced in the phantom; the primary and scatter dose-components emanating from the wedge, the wedge holder and the MLC; and the electron contamination dose-component. From the calculated and measured percentage depth dose (PDD) and off-center ratio (OCR) datasets, we may conclude that the convolution method can achieve accurate dose calculations even under MLC and/or wedge filtration.

Keywords: convolution method; X-ray spectra; dose kernels; wedge; multileaf collimation; MLC leaf-field output subtraction

Research highlights

Convolution methods are convenient for three-dimensional (3D) dose calculations, especially for an irregular-beam field with a non-uniform incident-beam intensity distribution. For a convolution method, we performed theoretical and experimental studies on 10-MV X-ray dose calculations in water phantoms with multileaf collimation (MLC) and/or wedge filtration using a linear accelerator equipped with a pair of upper jaws, a pair of lower jaws, an MLC and a wedge filter. The in-phantom dose calculation was performed by treating the phantom, the wedge filter, the wedge holder and the MLC as parts of a unified irradiated body. We can conclude that the convolution method can achieve accurate dose calculations even under MLC and/or wedge filtration.

Introduction

Megavoltage X-ray beams from linear accelerators are used for radiation therapy. The X-ray radiation produced in the X-ray target pass through a flattening filter that is symmetric with respect to the isocenter axis. The flattening filter makes the beam intensity distribution relatively uniform across the field. The filter is thickest in the middle

***Corresponding author:** Akira Iwasaki, 2-3-24 Shimizu, Hirosaki, Aomori 036-8254, Japan. Tel.: +172-33-2480; Email: fmcch384@ybb.ne.jp

Received 28 November 2016 *Revised* 9 February 2017 *Accepted* 25 February 2017 *Published* 10 March 2017

Citation: Iwasaki A, Kimura S, Sutoh K, Kamimura K, Sasamori M, Seino M, Komai F, Takagi M, Terashima S, Hosokawa Y, Saitoh H, Miyazawa M. 10-MV X-ray dose calculation in water for MLC and wedge fields using a convolution method with X-ray spectra reconstructed as a function of off-axis distance. J Radiol Imaging. 2017; 2(3):14-35. DOI: 10.14312/2399-8172.2017-4

and tapers off toward the edges; therefore, the X-ray spectrum is a function of the off-axis distance (radiation softening becomes more pronounced with increasing off-axis distance).

The dose at a point in a medium irradiated by an X-ray beam can be separated into three components. One is the primary dose, arising directly from primary photons that have not interacted with the medium before reaching the point. Another is the dose from scattered radiation originating from all points hit by primary photons in the medium. The last is the contamination dose, caused by electrons from the treatment head and air volume. With model-based algorithms, one can calculate the primary, scatter and contamination dose components separately. Convolution (or superposition) methods are in the class of model-based algorithms. They are convenient for three-dimensional (3D) dose calculations, especially for an irregular-beam field with a nonuniform incident-beam intensity distribution. As reviewed by Ahnesjö and Aspradakis [1], there are two kinds of convolution methods: one is a method that uses pencil-beam kernels, and the other is a method that uses point-dose kernels.

With respect to the latter convolution method, its numerical convolution is also called “the collapsed cone convolution” [2]. The present paper deals with a kind of collapsed cone convolution; however, it is to be emphasized that the dose calculation is performed using multiple primary- and scatter-dose kernels that are formed with the use of X-ray spectra reconstructed [3, 4] as a function of the off-axis distance.

For accurate primary and scatter dose calculations using convolution methods, Iwasaki [5] stipulated that the following four irradiation conditions be met: (a) a nondivergent beam, (b) a homogeneous phantom, (c) a beam attenuation coefficient along ray lines that is not a function of the depth and off-axis distance, and (d) an incident beam intensity that is uniform within the irradiation field and zero outside it. We have not yet dealt with the condition described in (a), Iwasaki, et al. [6] and Kimura, et al. [7] dealt with the condition described in (b) using inhomogeneous phantoms, proposing a correction factor for calculation of the primary dose within thorax-like phantoms, and also dealt with the condition described in (c) using X-ray spectra reconstructed as a function of the off-axis distance. In the present paper, we proposed a special correction factor for nonuniformity of the incident beam intensity described in the above (d) using multileaf collimator (MLC) and/or wedge fields. Because the MLC and wedge devices are usually made of high-Z materials, they can induce large changes in the incident beam intensity (also including the X-ray spectrum changes). The dose calculation simulations are performed using 10-MV X-ray beams, focusing on percentage depth dose (PDD) and off-center ratio (OCR) datasets in water phantoms.

Materials and methods

The physical parameters of the materials used in this study were evaluated using data tables published by Hubbell [8]. We used 10-MV X-ray beams from a linear accelerator (CL-2100C; Varian Medical Systems, Palo Alto, CA, USA). The treatment head contains pairs of upper and lower jaws; upper-1, -2 and lower-1, -2 (tungsten alloy) as the jaw collimator which is able to form a jaw field ≤ 40 × 40 cm^2 on the isocenter plane 100 cm distant from the source *(S)* (or the X-ray target). The treatment head also features an MLC (Millennium 120 Leaf; Varian Medical Systems) under the jaw-collimator device. Each leaf moves in the same direction as the lower jaws. We used wedge filters supplied by the manufacturer that are designed to be installed directly on the treatment head. The wedge filters, made of steel or lead alloys, form isodose angles of 15°, 30°, 45° and 60° in water and are mounted on an acrylic plate (wedge holder). Figure 1 diagrams the treatment head with an installed wedge. We let A_{jaw} and A_{MLC} denote the jaw and MLC fields, respectively, measured on the isocenter plane.

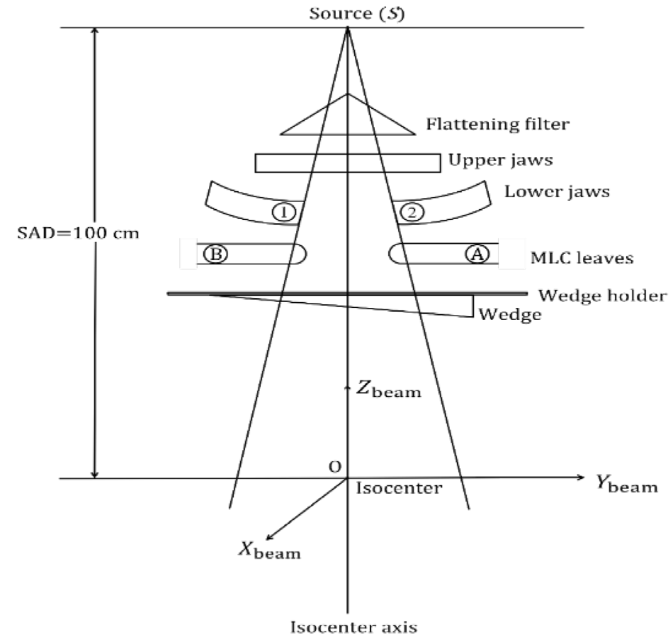

Figure 1 The treatment head is composed of a source *(S)*, a pair of upper jaws, a pair of lower jaws, and pairs of MLC leaves. A wedge filter can be placed on the treatment head. The orthogonal coordinate system with axes of X_{beam}, Y_{beam} and Z_{beam} setting the origins at the isocenter *(O)* was used for the dose calculation model.

Symbols and units

We use the following symbols and units in this paper: the spectra-related energies (E_N and ΔE_N) are expressed in MeV; the normalized set of reconstructed energy fluences (ψ's) is expressed in MeV^{-1}; the total in-air beam energy fluence $\left(\Psi_{total}^{in\_air}\right)$ is expressed in J/cm^2; the linear attenuation coefficients (e.g., μ_{water}, μ_{phan}, μ_{wedge}, μ_{MLC}, $\bar{\mu}_{med}$) for media are expressed in cm^{-1}; the lengths (Ξ, Η, ξ, η, R, r, R_0, etc.) are expressed in cm; the position vectors , ($\boldsymbol{L}_C$, $\boldsymbol{L}_{\Delta S}$, $\boldsymbol{L}_{\Delta V}^{phan}$, $\boldsymbol{L}_{\Delta V}^{wedge}$, $\boldsymbol{L}_{\Delta V}^{MLC}$, etc.), are expressed in cm; the primary and scatter dose components (D_{prim}^{phan}, D_{scat}^{phan}, etc.) are expressed in Gy; the beam water collision kerma (or the primary water collision kerma) components (K_{water}^{jaw} and K_{water}^{MLC}) are expressed in Gy; the dose kernels ($H_{1,2}$, $K_{1,2}$, h_{phan}, h_{wedge}, h_{MLC}, k_{phan}, k_{wedge}, k_{MLC}, etc.) are expressed in cm^{-3}; the volume element (ΔV) is expressed in cm^3; and the area element (ΔS) is expressed in cm^2.

Theoretical studies

We tried to calculate the dose at a point generally in an inhomogeneous phantom by treating the phantom, the wedge filter, the wedge holder and the MLC as parts of a unified irradiated body. For this calculation model, we used an orthogonal coordinate system of (X_{beam}, Y_{beam}, Z_{beam}) (Figures 1 and 2), setting the origin *(O)* at the isocenter. We denote the Z_{beam} axis as the line connecting the source *(S)* and the origin *(O)*, coinciding with the isocenter axis, and assume that the X_{beam} and Y_{beam} axes perpendicularly intersect the upper- and lower-jaw field edges, respectively, on the isocenter plane (Z_{beam} = 0 cm), calling this the "beam coordinate system". The MLC leaves move parallel to the Y_{beam} axis, in the same direction as that of the lower jaws. To calculate the expressions of equations 1−3 described in the following text to evaluate the dose at a point $P(X_C, Y_C, Z_C)$ in the phantom (Figure 2), we use two other coordinate systems in addition to the beam coordinate system (X_{beam}, Y_{beam}, Z_{beam}): one is the orthogonal coordinate system (x_v, y_v, z_v) with the origin at point P (it should be noted that the (x_v, y_v, z_v) coordinate system just coincides with the (X_{beam}, Y_{beam}, Z_{beam}) coordinate system when point P coincides with the isocenter *(O)*; and the other is the polar coordinate system (r', φ, θ) directly associated with the (x_v, y_v, z_v) coordinate system.

Dose calculation principle

The dose calculation was performed using a convolution method that utilizes special types of in-water primary and scatter dose kernels ($H_{1,2}$ and $K_{1,2}$ (see Appendix A)), formed for the energy bins of X-ray spectra [3, 4] reconstructed as a function of the off-axis distance. It should be noted that the usual number of energy bins is approximately ten, and that the reconstructed X-ray spectra can reasonably be applied [4] to media with a wide range of effective *Z* numbers (e.g., from water to lead). When applying the density scaling theorem [9-11] to the in-water primary and scatter dose kernels again under the conditions that the phantom, wedge filter, wedge holder and MLC are treated as parts of a unified irradiated body, the use of the relative electron density (ρ_e) is not feasible. This is because the effective *Z* numbers of the media within the unified irradiated body are quite different from one another, depending on the energy bins of the reconstructed X-ray spectra. Thus, we propose to use a factor of $\bar{\mu}_{med}/\mu_{water}$ (the relative attenuation factor) for the medium of each volume element within the unified irradiated body, where μ_{med} and μ_{water} are the linear attenuation coefficients of the volume element material and water, respectively, and are determined by each of the energy bins of the reconstructed X-ray spectra. For the volume elements existing along a line connecting two points, we propose to use the mean relative attenuation factor, μ_{med}/μ_{water} instead of using the mean relative electron density ($\bar{\rho}_e$). It should be noted that the linear attenuation coefficients μ_{med}, μ_{water} and $\bar{\mu}_{med}$ generally change with the energy bin of the reconstructed X-ray spectra, whereas ρ_e or $\bar{\rho}_e$ does not. In addition, for water-like media, we can assume $\rho_e = \mu_{med}/\mu_{water}$ and $\bar{\rho}_e = \bar{\mu}_{med}/\mu_{water}$ for any energy bin. This method of using the linear attenuation coefficients may be effective for handling the scatter dose kernels. However, it may not be effective for handling the primary dose kernels because the primary dose is caused by the secondary electrons generated by the interaction between the volume element and the primary photons. The secondary electrons do not have a strong relationship with photon attenuation from the standpoint of energy deposition in media.

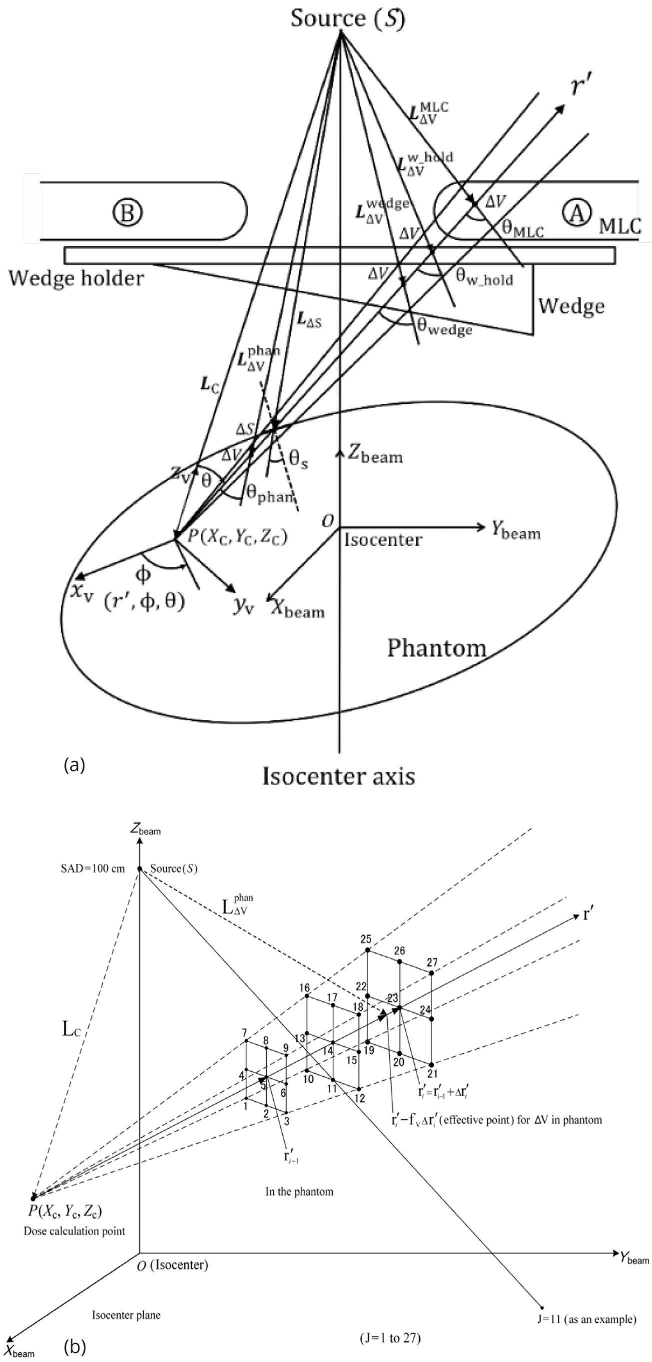

Figure 2 (a) Diagram showing how to calculate the dose at point P in the phantom, where wedge and MLC devices are generally used; the primary and scatter doses emanate from the volume elements (ΔV's) in the phantom, wedge filter, wedge holder and MLC (unified irradiated body); the electron contamination dose emanates from the area element (ΔS) on the phantom surface; $\boldsymbol{L}_C, \boldsymbol{L}_{\Delta V}^{phan}, \boldsymbol{L}_{\Delta V}^{wedge}, \boldsymbol{L}_{\Delta V}^{w\_hold}, \boldsymbol{L}_{\Delta V}^{MLC}$ and $\boldsymbol{L}_{\Delta s}$ are the position vectors; and θ_{phan}, θ_{wedge}, θ_{w_hold}, θ_{MLC} and θ_s are the angles (it should be emphasized that the (x_v, y_v, z_v) coordinate system becomes the (X_{beam}, Y_{beam}, Z_{beam}) coordinate system when point P coincides with the isocenter *(O)*; (b) Diagram showing how to determine the effective point within a volume element (ΔV) in the phantom as $(r_i' - f_V \Delta r_i')$ with f_V = 0.415 for primary dose calculations, and with f_V = 0.01 for scatter dose calculations, also showing how to set OPF_J data (J=1,2,..., J_{max}) on the isocenter plane.

Figure 2 also shows a quadrangular pyramid in polar coordinates, whose apex is situated at point P. It shows how to calculate the primary, scatter and electron contamination doses delivered to point P, where the primary and scatter doses arise from the volume elements (ΔV's) in the unified irradiated body; and the electron contamination dose arises from the area element ΔS. Regarding to the volume elements (ΔV's) and area elements (ΔS's, we employed a series of θ, Δθ, ϕ, $\Delta\phi$, r' and Δr' data (see Appendix B). For the convolution dose calculation, (a) we used a set of X-ray spectra reconstructed as a function of the off-axis distance, letting the bin energies be E_N (N = 1, 2,..., $N_{\max}$ with $N_{\max} \cong 10$) for each off-axis distance; (b) we used primary dose kernels (h_{phan}, h_{wedge}, $h_{\text{w\_hold}}$ and h_{MLC}) and scatter dose kernels (k_{phan}, k_{wedge}, $k_{\text{w\_hold}}$ and k_{MLC}) as a function of E_N for the volume and area elements, where these dose kernels are rebuilt from the in-water primary and scatter dose kernels ($H_{1,2}$ and $K_{1,2}$); and (c) we estimated values of $K_{\text{water}}^{\text{jaw}}$ and $K_{\text{water}}^{\text{MLC}}$ as a function of E_N for each of the volume and area elements.

For dose calculation generally under the presence of the MLC and a wedge filter, we divided the dose to point P into nine components: (a) the primary and scatter doses ($D_{\text{prim}}^{\text{phan}}$ and $D_{\text{scat}}^{\text{phan}}$) produced in the phantom; (b) the primary and scatter doses ($D_{\text{prim}}^{\text{wedge}}$ and $D_{\text{scat}}^{\text{wedge}}$) emanating from the wedge filter; (c) the primary and scatter doses ($D_{\text{prim}}^{\text{w\_hold}}$ and $D_{\text{scat}}^{\text{w\_hold}}$) emanating from the wedge holder; (d) the primary and scatter doses ($D_{\text{prim}}^{\text{MLC}}$ and $D_{\text{scat}}^{\text{MLC}}$) emanating from the MLC; and (e) the contamination dose D_{cont} caused by the electrons emanating from the treatment head and the air volume.

It should be noted that this calculation method does not strictly take into account the primary and scatter doses due to the secondary electrons and scattered photons, respectively, produced in the upper and lower jaws. Instead, it treats the radiation reflected from the jaws as a small increase in the in-air beam intensity using a jaw radiation reflection factor [6] that lies outside the jaw field, as described by a Monte Carlo simulation model [12] stating that the photons scattered from the jaws can be ignored when estimating the in-air beam intensity within the jaw field.

Within the unified irradiated body, we set the beam water collision kerma ($K_{\text{water}}^{\text{jaw}}$ or $K_{\text{water}}^{\text{MLC}}$) to act on the dose kernel at each ΔV or ΔS element point. When the beam water collision kerma should be determined based on the open jaw field without the MLC device, we denote it as $K_{\text{water}}^{\text{jaw}}$. When the beam water collision kerma should be determined based on the open MLC field under a given jaw field, we denote it as $K_{\text{water}}^{\text{MLC}}$.

Next, we describe the dose calculation approaches using position vectors, generally taking an irradiation case in which both wedge and MLC devices are installed in a jaw field (Figure 2a). We let $\boldsymbol{L}_{\text{c}}$ denote the position vector to a dose calculation point P, drawn from the source *(S)*; and $\boldsymbol{L}_{\Delta V}^{\text{phan}}$, $\boldsymbol{L}_{\Delta V}^{\text{wedge}}$, $\boldsymbol{L}_{\Delta V}^{\text{w\_hold}}$ and $\boldsymbol{L}_{\Delta V}^{\text{MLC}}$ denote the position vectors to volume elements (ΔV's) in the phantom, wedge filter, wedge holder and MLC, respectively, drawn from the source *(S)*; and $\boldsymbol{L}_{\Delta S}$ denote the position vector to an area element (ΔS) on the phantom surface, drawn from the source *(S)*. Then the primary, scatter and electron contamination dose calculations are performed using the follow approaches.

(a) The primary dose calculation approach:

$$D_{\text{prim}}\left(\boldsymbol{L}_{\text{c}}\right)=\sum_{N=1}^{N_{\max}}\Big[\sum_{\Delta V} h_{phan}\left(L_c-L_{\Delta V}^{phan};E_n\right)\cdot K_{water}^{MLC}\left(L_{\Delta V}^{phan};E_N\right)_{Phan}\cdot\frac{\mu_{phan}\left(L_{\Delta V}^{phan};E_N\right)}{\mu_{water}\left(E_N\right)}\Delta V\left(L_{\Delta V}^{phan}\right)+\sum_{\Delta V} h_{wedge}\left(\boldsymbol{L}_{\text{c}}-\boldsymbol{L}_{\Delta V}^{\text{wedge}};E_N\right)\cdot K_{\text{water}}^{\text{jaw}}\left(\boldsymbol{L}_{\Delta V}^{\text{wedge}};E_N\right)_{\text{wedge}}\cdot\frac{\mu_{\text{wedge}}\left(\boldsymbol{L}_{\Delta V}^{\text{wedge}};E_N\right)}{\mu_{\text{water}}\left(E_N\right)}\Delta V\left(\boldsymbol{L}_{\Delta V}^{\text{wedge}}\right)$$

$$+\sum_{\Delta V} h_{w\_hold}\left(\boldsymbol{L}_{\text{c}}-\boldsymbol{L}_{\Delta V}^{\text{w\_hold}};E_N\right)\cdot K_{\text{water}}^{\text{jaw}}\left(\boldsymbol{L}_{\Delta V}^{\text{w\_hold}};E_N\right)_{\text{w\_hold}}\cdot\frac{\mu_{\text{w\_hold}}\left(\boldsymbol{L}_{\Delta V}^{\text{w\_hold}};E_N\right)}{\mu_{\text{water}}\left(E_N\right)}\Delta V\left(\boldsymbol{L}_{\Delta V}^{\text{w\_hold}}\right)+\sum_{\Delta v} h_{MLC}\left(\boldsymbol{L}_{\text{c}}-\boldsymbol{L}_{\Delta V}^{\text{MLC}};E_N\right)\cdot K_{\text{water}}^{\text{jaw}}\left(\boldsymbol{L}_{\Delta V}^{\text{MLC}};E_N\right)_{\text{MLC}}\cdot\frac{\mu_{\text{MLC}}\left(\boldsymbol{L}_{\Delta V}^{\text{MLC}};E_N\right)}{\mu_{\text{water}}\left(E_N\right)}\Delta V\left(\boldsymbol{L}_{\Delta V}^{\text{MLC}}\right)\Big], \tag{1}$$

where $K_{\text{water}}^{\text{MLC}}$ and $K_{\text{water}}^{\text{jaw}}$ express the beam water collision kermas at the corresponding volume elements (ΔV's), respectively, in the phantom and in the wedge or MLC device (equations 40-42, 46).

(b) The scatter dose calculation approach:

$$D_{\text{scat}}\left(\boldsymbol{L}_{\text{c}}\right)=\sum_{N=1}^{N_{\max}}\Bigg[\sum_{\Delta V} k_{\text{phan}}\left(\boldsymbol{L}_{\text{c}}-\boldsymbol{L}_{\Delta V}^{\text{phan}};E_N\right)\cdot K_{\text{water}}^{\text{MLC}}\left(\boldsymbol{L}_{\Delta V}^{\text{phan}};E_N\right)_{\text{phan}}\cdot\frac{\mu_{\text{phan}}\left(\boldsymbol{L}_{\Delta V}^{\text{phan}};E_N\right)}{\mu_{\text{water}}\left(E_N\right)}\Delta V\left(\boldsymbol{L}_{\Delta V}^{\text{phan}}\right)+\sum_{\Delta V} k_{\text{wedge}}\left(\boldsymbol{L}_{\text{c}}-\boldsymbol{L}_{\Delta V}^{\text{wedge}};E_N\right)\cdot K_{\text{water}}^{\text{jaw}}\left(\boldsymbol{L}_{\Delta V}^{\text{wedge}};E_N\right)_{\text{wedge}}\cdot\frac{\mu_{\text{wedge}}\left(\boldsymbol{L}_{\Delta V}^{\text{wedge}};E_N\right)}{\mu_{\text{water}}\left(E_N\right)}\Delta V\left(\boldsymbol{L}_{\Delta V}^{\text{wedge}}\right)$$

$$+\sum_{\Delta V} k_{\text{w\_hold}}\left(\boldsymbol{L}_{\text{c}}-\boldsymbol{L}_{\Delta V}^{\text{w\_hold}};E_N\right)\cdot K_{\text{water}}^{\text{jaw}}\left(\boldsymbol{L}_{\Delta V}^{\text{w\_hold}};E_N\right)_{\text{w\_hold}}\cdot\frac{\mu_{\text{w\_hold}}\left(\boldsymbol{L}_{\Delta V}^{\text{w\_hold}};E_N\right)}{\mu_{\text{water}}\left(E_N\right)}\Delta V\left(\boldsymbol{L}_{\Delta V}^{\text{w\_hold}}\right)+\sum_{\Delta V} k_{\text{MLC}}\left(\boldsymbol{L}_{\text{c}}-\boldsymbol{L}_{\Delta V}^{\text{MLC}};E_N\right)\cdot K_{\text{water}}^{\text{jaw}}\left(\boldsymbol{L}_{\Delta V}^{\text{MLC}};E_N\right)_{\text{MLC}}\cdot\frac{\mu_{\text{MLC}}\left(\boldsymbol{L}_{\Delta V}^{\text{MLC}};E_N\right)}{\mu_{\text{water}}\left(E_N\right)}\Delta V\left(\boldsymbol{L}_{\Delta V}^{\text{MLC}}\right)\Bigg], \tag{2}$$

(c) The contamination dose calculation approach:

$$D_{\text{cont}}\left(\boldsymbol{L}_{\text{c}}\right)=\sum_{N=1}^{N_{\max}}\Bigg[\sum_{\Delta S} h_{\text{phan}}\left(\boldsymbol{L}_{\text{c}}-\boldsymbol{L}_{\Delta S};E_N\right)\cdot K_{\text{water}}^{\text{MLC}}\left(\boldsymbol{L}_{\Delta S};E_N\right)_{\text{phan}}\cdot G\left(A_{\text{jaw}}\right)\cdot\Gamma_1\left(T_{\text{eff}}\left(E_N\right);E_N\right)\cdot\Gamma_2\left(\boldsymbol{L}_{\text{c}}-\boldsymbol{L}_{\Delta S}\right)\cdot\Delta S\left(\boldsymbol{L}_{\Delta S}\right)\cos\theta_{\text{S}},\Bigg] \tag{3}$$

where $K_{\text{water}}^{\text{MLC}}$ express the beam water collision kerma at the corresponding phantom surface element (ΔS) (equation 43); ΔS is defined as the size of the area element on the phantom surface, which faces the source *(S)* without interception by the phantom; θ_{S} is the angle between the normal vector line on the ΔS surface and the negative vector of $\boldsymbol{L}_{\Delta S}$ $(0 \le \theta_{\text{S}} \le \pi/2)$; $G(A_{\text{jaw}})$ expresses the electron contamination factor as a function of the jaw field (A_{jaw}) [6, 7]. Γ_1 and Γ_2 are introduced to improve the G function, which can apply only to open jaw fields and only to electrons streaming along the ray lines emanating from the source *(S)*.

Γ_1 represents the degree of attenuation of the contaminant electrons when penetrating the MLC and wedge filter along the position vector $\boldsymbol{L}_{\Delta S}$. Let Γ_1 be formulated using penetration features of the secondary electrons produced by E_N photons as

$$\Gamma_1(T_{\text{eff}}(E_N);E_N)=H_1(T_{\text{eff}}(E_N),0;E_N)/H_1(0,0;E_N)\quad,\tag{4}$$

where $H_1(\Xi, R; E_N)$ expresses the in-water forward primary dose kernel to point (Ξ, R) produced by E_N photons (refer to Appendix A); and $T_{\text{eff}}(E_N)$ is the total effective thickness for the MLC and wedge devices, evaluated along the position vector $\boldsymbol{L}_{\Delta S}$ as a function of E_N. It is calculated as

$$T_{\text{eff}}(E_N)=\left[\mu_{\text{MLC}}(E_N)T_{\text{MLC}}+\mu_{\text{wedge}}(E_N)T_{\text{wedge}}+\mu_{\text{w\_hold}}(E_N)T_{\text{w\_hold}}\right]/\ \mu_{\text{water}}(E_N)\quad,\tag{5}$$

where $\mu_{\text{MLC}}(E_N)$, $\mu_{\text{wedge}}(E_N)$, $\mu_{\text{w\_hold}}(E_N)$ and $\mu_{\text{water}}(E_N)$ are the linear attenuation coefficients of the MLC, wedge filter, wedge holder and water, respectively, for E_N photons; and T_{MLC}, T_{wedge} and $T_{\text{w\_hold}}$ are the thicknesses of the MLC, wedge filter and wedge holder, respectively, measured along the position vector $\boldsymbol{L}_{\Delta S}$.

Γ_2 is introduced to improve the accuracy of the calculation at points very near the phantom surface [7], to take into account the dose delivered by the contaminant electrons coming across the ray lines. For phantoms constructed of water-like media, we express Γ_2 as

$$\Gamma_2(\boldsymbol{L}_c-\boldsymbol{L}_{\Delta S})=1+175\exp\left(-200\bar{\rho}_e\left|\boldsymbol{L}_c-\boldsymbol{L}_{\Delta S}\right|\right)\ ,\tag{6}$$

where $\bar{\rho}_e$ is the relative electron density averaged between point P and the ΔS center (however, it has been found [13-15] that the contamination dose does not vary simply in proportion to the beam water collision kerma of $K_{\text{water}}^{\text{jaw}}$).

In regard to the calculated dose to point $P(X_C, Y_C, Z_C)$ in the phantom (Figure 2), it can be understood that the primary and scatter doses emanating from the volume elements in the phantom are generally composed of forward and backward dose components, that the primary and scatter doses emanating from volume elements in the wedge and MLC devices are composed only of forward dose components because these devices are placed relatively far above the phantom, and that the contamination dose is generally composed of forward and backward dose components. Appendix A defines in-water primary and scatter dose kernels as $H_1(\Xi, R; E_N)$, $H_2(\mathrm{H}, R; E_N)$, $K_1(\Xi, R; E_N)$ and $K_2(\mathrm{H}, R; E_N)$ using orthogonal coordinates (Ξ, R) and (H, R) for incident E_N photons.

Next, we examine the dose kernels of h_{phan}, h_{wedge}, $h_{\text{w\_hold}}$, h_{MLC}, k_{phan}, k_{wedge}, $k_{\text{w\_hold}}$ and k_{MLC} (equations 1-3) used in the unified irradiated body. According to the aforementioned density scaling theorem, the coordinates of ξ, η, r, ξ_s, η_s and r_s shown in Figure 3 can be converted to the in-water coordinates as:

$$\Xi=\left[\bar{\mu}_{\text{med}}(E_N)/\mu_{\text{water}}(E_N)\right]\xi,\ H=\left[\bar{\mu}_{\text{med}}(E_N)/\mu_{\text{water}}(E_N)\right]\eta,\ R=\left[\bar{\mu}_{\text{med}}(E_N)/\mu_{\text{water}}(E_N)\right]r$$

$$\Xi_s=\left[\bar{\mu}_{\text{med}}(E_N)/\mu_{\text{water}}(E_N)\right]\xi_s,\ H_s=\left[\bar{\mu}_{\text{med}}(E_N)/\mu_{\text{water}}(E_N)\right]\eta_s\ \text{and}\ R_s=\left[\bar{\mu}_{\text{med}}(E_N)/\mu_{\text{water}}(E_N)\right]r_s$$

Then, the dose kernels in equations 1-3 can be evaluated by employing the in-water dose kernels ($H_{1,2}$ and $K_{1,2}$) as follows (also refer to the angles of θ_{phan}, θ_S, θ_{wedge}, $\theta_{\text{w\_hold}}$ and θ_{MLC} in Figure 2):

(a) h_{phan} in equation 1 is one of the following two kernels:

$$h_1(\xi,r;E_N)_{\text{phan}}=\left(\frac{\bar{\mu}_{\text{med}}(E_N)}{\mu_{\text{water}}(E_N)}\right)^2\cdot H_1(\Xi,R;E_N)\cdot F_{\text{hetero}},\ \text{for}\ \theta_{\text{phan}}\le\pi/2\tag{7}$$

$$h_2(\xi,r;E_N)_{\text{phan}}=\left(\frac{\bar{\mu}_{\text{med}}(E_N)}{\mu_{\text{water}}(E_N)}\right)^2\cdot H_2(H,R;E_N)\cdot F_{\text{hetero}},\ \text{for}\ \theta_{\text{phan}}>\pi/2\tag{8}$$

where $\bar{\mu}_{\text{med}}(E_N)$ is evaluated along the line connecting P and the effective point within the ΔV element; and F_{hetero} is a correction factor [6, 7] for phantom heterogeneity. This correction factor is simply used only for forward primary dose calculations, not as a function of E_N. We should set $F_{\text{hetero}}=1$ for homogeneous phantoms.

(b) k_{phan} in equation 2 is one of the following two kernels:

$$k_1(\xi,r;E_N)_{\text{phan}}=\left(\frac{\bar{\mu}_{\text{med}}(E_N)}{\mu_{\text{water}}(E_N)}\right)^2\cdot K_1(\Xi,R;E_N),\ \text{for}\ \theta_{\text{phan}}\le\pi/2\tag{9}$$

$$k_2(\eta,r;E_N)_{\text{phan}}=\left(\frac{\bar{\mu}_{\text{med}}(E_N)}{\mu_{\text{water}}(E_N)}\right)^2\cdot K_2(H,R;E_N),\ \text{for}\ \theta_{\text{phan}}>\pi/2\tag{10}$$

(c) h_{phan} in equation 3 is one of the following two kernels:

$$h_1(\xi_s,r_s;E_N)_{\text{phan}}=\left(\frac{\bar{\mu}_{\text{med}}(E_N)}{\mu_{\text{water}}(E_N)}\right)^2\cdot H_1(\Xi_s,R_s;E_N),\ \text{for}\ \theta_s\le\pi/2\ ,\tag{11}$$

$$h_2(\eta_s,r_s;E_N)_{\text{phan}}=\left(\frac{\bar{\mu}_{\text{med}}(E_N)}{\mu_{\text{water}}(E_N)}\right)^2\cdot H_2(H_s,R_s;E_N),\ \text{for}\ \theta_s>\pi/2\ ,\tag{12}$$

where $\bar{\mu}_{\text{med}}(E_N)$ is evaluated along the line connecting P and the center of ΔS.

(d) h_{wedge} and k_{wedge} (used as $\theta_{\text{wedge}}<\pi/2$) in equations 1 and 2 are, respectively,

$$h_1(\xi,r;E_N)_{\text{wedge}}=\left(\frac{\bar{\mu}_{\text{med}}(E_N)}{\mu_{\text{water}}(E_N)}\right)^2\cdot H_1(\Xi,R;E_N)\cdot F_{\text{wedge\_p}}\ ,\tag{13}$$

$$k_1(\xi,r;E_N)_{\text{wedge}}=\left(\frac{\bar{\mu}_{\text{med}}(E_N)}{\mu_{\text{water}}(E_N)}\right)^2\cdot K_1(\Xi,R;E_N)\cdot F_{\text{wedge\_s}}\ ,\tag{14}$$

where $F_{\text{wedge\_p}}$ and $F_{\text{wedge\_s}}$ are the correction factors, respectively, for the calculation of the primary and scatter dose components, not as a function of E_N. We express them as

$$F_{\text{wedge\_p}}=\alpha_{\text{wedge\_p}}\cdot T_{\text{wedge}}^{\ \beta_{\text{wedge\_p}}}\ ,\tag{15}$$

$$F_{\text{wedge\_s}}=1/\left[\gamma_{\text{wedge\_s}}\cdot\left(1+\alpha_{\text{wedge\_s}}\cdot T_{\text{wedge}}^{\ \beta_{\text{wedge\_s}}}\right)\right]\ ,\tag{16}$$

with $T_{wedge}=\sqrt{\Xi^2+R^2}$, where α_{wedge_p} = 2.5 × 10^{-2}, β_{wedge_p} = 0.5, α_{wedge_p} = 7.0 × 10^{-8}, β_{wedge_p} = 0.5 and γ_{wedge_s} = 50 for each of the 15°, 30°, 45° and 60° wedges (wedge types 1–4) (these values, without units, were derived by comparing the calculated and measured dose datasets).

(e) h_{w_hold} and k_{w_hold} (used as $\theta_{w\_hold} < \pi/2$) in equations 1 and 2 are, respectively,

$$h_1(\xi,r;E_N)_{w\_hold}=\left(\frac{\bar{\mu}_{med}(E_N)}{\mu_{water}(E_N)}\right)^2\cdot H_1(\Xi,R;E_N)\cdot F_{wedge\_p}\ , \quad (17)$$

$$k_1(\xi,r;E_N)_{w\_hold}=\left(\frac{\bar{\mu}_{med}(E_N)}{\mu_{water}(E_N)}\right)^2\cdot K_1(\Xi,R;E_N)\cdot F_{wedge\_s}\ , \quad (18)$$

(f) h_{MLC} and k_{MLC} (used as $\theta_{MLC} < \pi/2$) in equations 1 and 2 are, respectively,

$$h_1(\xi,r;E_N)_{MLC}=\left(\frac{\bar{\mu}_{med}(E_N)}{\mu_{water}(E_N)}\right)^2\cdot H_1(\Xi,R;E_N)\cdot F_{MLC\_p}\ , \quad (19)$$

$$k_1(\xi,r;E_N)_{MLC}=\left(\frac{\bar{\mu}_{med}(E_N)}{\mu_{water}(E_N)}\right)^2\cdot K_1(\Xi,R;E_N)\cdot F_{MLC\_s}\ , \quad (20)$$

where F_{MLC_p} and F_{MLC_s} are the correction factors, respectively, for the calculation of the primary and scatter dose components emanating from the MLC, not as functions of E_N. We express them as

$$F_{MLC\_p}=\alpha_{MLC\_p}\cdot T_{MLC}^{\beta_{MLC\_p}}\ , \quad (21)$$

$$F_{MLC\_s}=1/\left[\gamma_{MLC\_s}\cdot\left(1+\alpha_{MLC\_s}\cdot T_{MLC}^{\beta_{MLC\_s}}\right)\right]\ , \quad (22)$$

with $T_{MLC}=\sqrt{\Xi^2+R^2}$, where we let

$\alpha_{(MLC\_p)}=1\times10^{-3}, \beta_{(MLC\_p)}=1.5, \alpha_{(MLC\_s)}=100, \beta_{(MLC\_s)}=1.5$ and $\gamma_{(MLC\_s)}=1.0$

(these values without units were derived by comparing the calculated and measured dose datasets).

Modeling the jaw collimator, MLC and wedge devices

The jaw collimator, MLC and wedge devices are 3D objects (Figure 4a). However, to simplify the calculation of the in-air beam intensity with an open jaw field or with an open MLC field under a jaw field, and to also simplify the calculation of the dose that the phantom receives from the MLC and wedge, we treated the jaws, MLC and wedge as two-dimensional (2D) structures. That is, we treated them as plates with no geometrical thickness (Figure 4b). The following describes the details of the jaws, MLC and wedge plates:

(a) The jaw collimator is simulated by four plates that are perpendicular to the isocenter axis. They are located at four positions: Z_{beam} = Z_{upper_1} (≅72.0 cm), Z_{beam} = Z_{upper_2} (≅ 72.0 cm), Z_{beam} = Z_{lower_1} (≅ 63.3 cm) and Z_{beam} = Z_{lower_2} (≅ 63.3 cm). The Z_{upper_1} and Z_{upper_2} positions coincide with the corresponding top edges of the upper-1 and -2 jaws, respectively, and the Z_{lower_1} and Z_{lower_2} positions coincide with the corresponding top edges of the lower_1 and _2 jaws, respectively. We assume that these four plates form the same irradiation field on the isocenter plane as the real jaws do, and that the radiation emanating from the source *(S)* is perfectly shielded by the plates. This replacement is performed [6] to calculate in a simple manner the in-air beam intensity caused by the extended radiation source

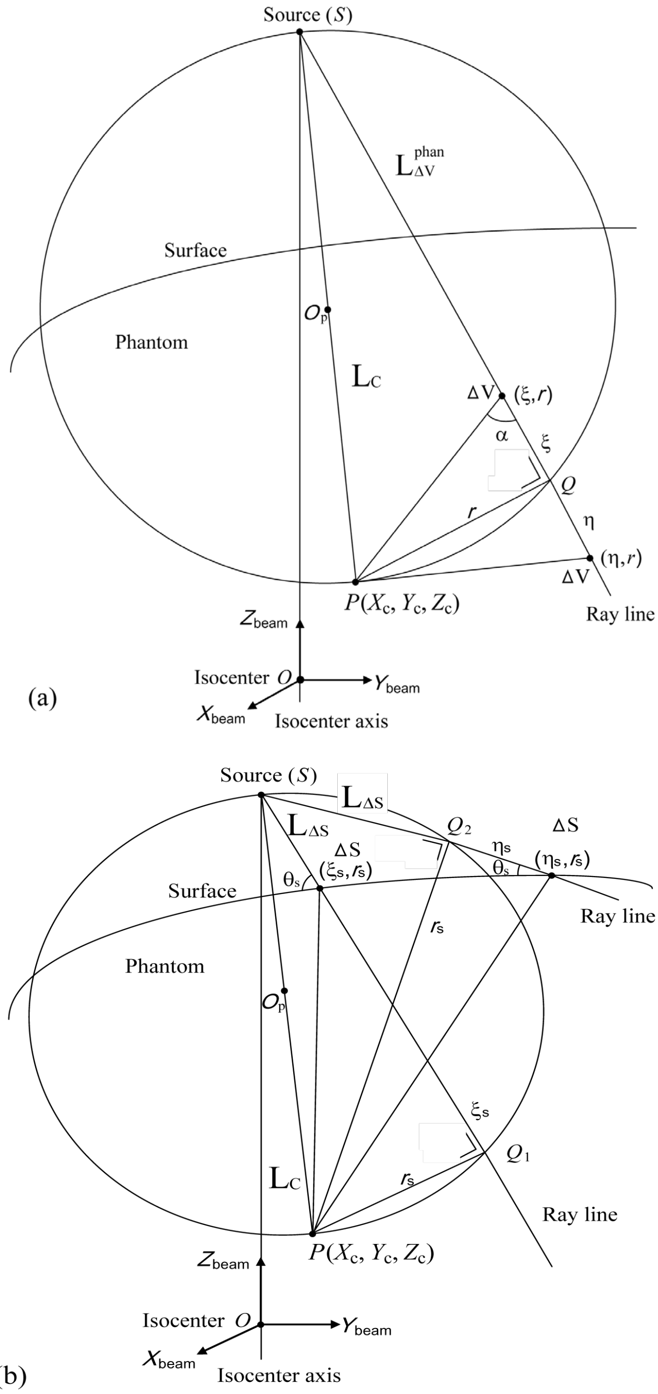

Figure 3 (a) Diagram showing how to calculate the primary and scatter doses at point $P(X_C, Y_C, Z_C)$ in a phantom. Point O_p is situated at the middle of the line connecting the source *(S)* and point *P*. A sphere is drawn with the diameter of *SP*, with the center set at point O_p. Points (ξ, *r*) and (*η*, *r*) are, respectively, inside and outside the sphere; (b) Diagram showing how to calculate the contamination dose at point $P(X_C, Y_C, Z_C)$ in a phantom. Point O_p is situated at the middle of the line connecting the source *(S)* and point *P*. A sphere is drawn with the diameter of *SP*, with the center set at point O_p. Points (ξ_s, r_s) and (η_s, r_s) are, respectively, inside and outside the sphere.

on the X-ray target plane and the extended radiation source on the flattening-filter plane. It should be noted that this replacement causes a slight inconvenience for the calculation of the in-air beam intensity outside the jaw field (refer to the circle mark in Figure 5b as described later).

(b) The MLC is simulated by a plate perpendicular to the isocenter axis at the position $Z_{beam} = Z_{MLC}$ (= 53.7 cm, which was determined by analyzing the measured MLC-S_c datasets shown in Figure 6 below). We let the plate form the same MLC field as the MLC does on the isocenter plane, corresponding to the MLC effective thicknesses along ray lines emanating from the source *(S)*. This dataset is used to calculate the in-air beam intensity for the open MLC field. It is also used for calculating the dose that the phantom receives from the MLC.

(c) Each of the wedges (15°, 30°, 45° and 60°) and their 0.2 cm acrylic holder are replaced with a plate perpendicular to the isocenter axis at the fixed position $Z_{beam} = Z_{wedge}$ (= 42.4 cm), which is the same as the position of the boundary surface of the wedge and its holder. We let the plate form the wedge field as the wedge device does on the isocenter plane, corresponding to the wedge filter and wedge holder thicknesses along ray lines emanating from the source *(S)*. This dataset is used to calculate the dose that the phantom receives from the wedge device and the in-air beam intensity under the wedge-filtered jaw or MLC field.

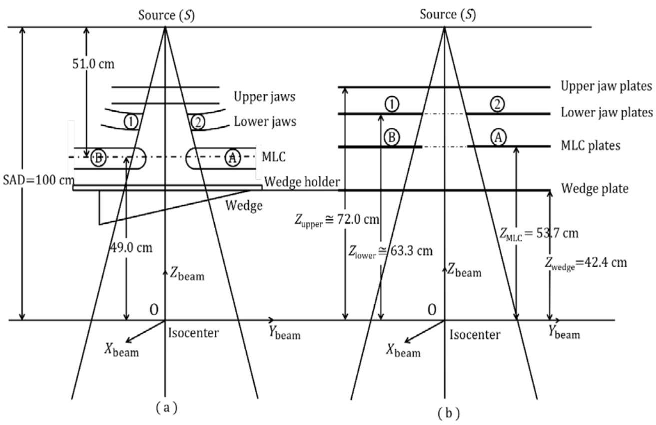

Figure 4 Drawings of geometrical arrangement for the upper and lower jaws, the MLC and the wedge for (a) the three-dimensional structural devices and for (b) the simplified two-dimensional plate devices.

In-air output factor calculation for open MLC fields

We describe how to calculate the in-air beam intensity for an open MLC field under a given jaw field (without wedge filtration). The calculation is based on the MLC leaf-field output subtraction method [16] at the 15th ICCR. The details are; Zhu and Bjärngard [17] and Zhu and colleagues [18-20] introduced the 2D Gaussian-source model for the extended radiation source only with a flattening filter to calculate the in-air output factor (S_c) [21, 22] for open jaw or MLC fields. Later, Iwasaki and colleagues [6] proposed the use of this model not only for the flattening filter but also for the X-ray target (or the source *(S)*). It was found that using the two extended radiation sources was effective, even around a zero-area jaw field under conditions of lateral electron disequilibrium. We propose using the two extended radiation sources model to calculate the in-air output factor (OPF_{in_air}) for an open MLC field under a given jaw field by subtracting the in-air output reduction caused by setting the MLC field to the jaw field from the in-air output for the open jaw field (let the in-air output reduction be designated the negative or "black" in-air output). This calculation method can take into account the delicate in-air output variations caused by the MLC leaf curvature and chamfers at the leaf end and the MLC interleaf X-ray leakage.

Figure 5 shows the calculation of the OPF_{in_air} factor at a point $Q(X_0,Y_0)$ on the isocenter plane for an open MLC field (A_{MLC}) under a given jaw field (A_{jaw}), where Figures 5a, b are drawn for the cases where point Q is inside and outside the A_{jaw} field, respectively. An extended radiation source exists around point O_S (coinciding with the center of the X-ray target) on the source plate; and another extended radiation source is assumed to exist around point O_F at the intersection of the flattening-filter plate and the ray line connecting points O_S and Q. On the isocenter plane, we introduce a special field called a black MLC field (A_{MLC}^{black}),

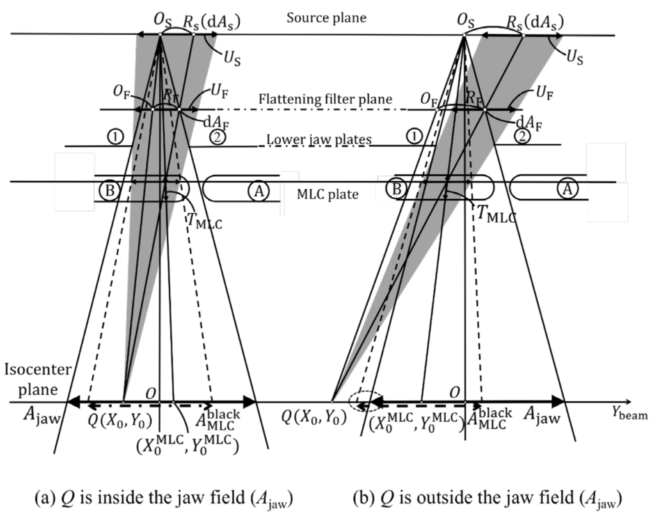

Figure 5 Schematic diagrams showing how to calculate the OPF_{in_air} factor for a point Q on the isocenter plane when (a) point Q is inside the A_{jaw} field, and when (b) point Q is outside the A_{jaw} field (note that, as indicated by the circle mark, the A_{MLC}^{black} field extends from the A_{jaw} field edge). It should be noted that the dashed lines are drawn only by taking into account the positions of the lower jaw plates, and that, in like manner, another set of dashed lines should also be utilized by taking into account the positions of the upper jaw plates.

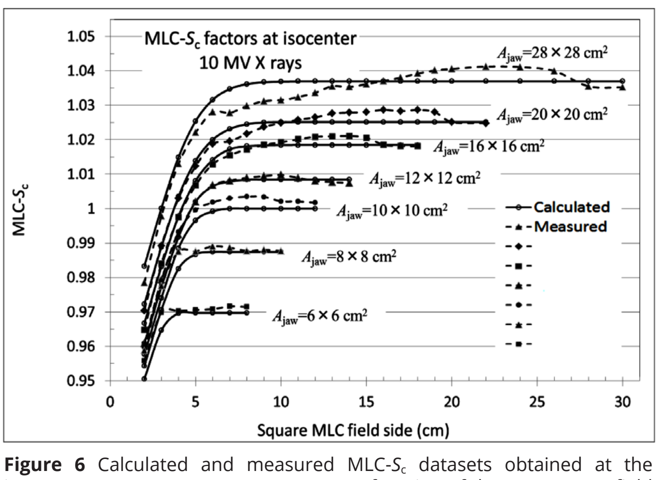

Figure 6 Calculated and measured MLC-S_c datasets obtained at the isocenter (X_{beam} = 0 cm,Y_{beam} = 0 cm) as a function of the square MLC field side under each of the square A_{jaw} fields of 6 × 6-28 × 28 cm².

which is used to evaluate the amount of negative (or black) in-air output, (where the dashed lines in Figures 5a, b are drawn by taking into account the positions of the lower jaw plates (in like manner, another set of dashed lines should also be utilized by taking into account the positions of the upper jaw plates)). It should be emphasized that, if point Q is outside the A_{jaw} field, the $A_{\mathrm{MLC}}^{\mathrm{black}}$ field does not contain point Q. In this case, as indicated by the circle mark in Figure 5b, the $A_{\mathrm{MLC}}^{\mathrm{black}}$ field extends beyond the A_{jaw} field edge. Such an extended region is caused by the treatment of the 2D jaw-collimator plates (the irradiation geometry tells us that, if the real 3D jaw collimator can be utilized, no such large $A_{\mathrm{MLC}}^{\mathrm{black}}$ fields can be generated).

We normalize the $\mathrm{OPF}_{\mathrm{in\_air}}$ factor to unity at the isocenter with an open jaw field of A_{jaw} = 10 × 10 cm^2 (= 10 × 10$_{\mathrm{iso}}$), whose center coincides with the isocenter. Then, the $\mathrm{OPF}_{\mathrm{in\_air}}$ factor at point Q(X_0, Y_0) for an open A_{MLC} field under a given A_{jaw} field can be calculated as

$$\mathrm{OPF}_{\mathrm{in\_air}}\left(X_0,Y_0;A_{\mathrm{MLC}},A_{\mathrm{jaw}}\right)=\left[\frac{H_{\mathrm{jaw}}\left(X_0,Y_0;A_{\mathrm{jaw}}\right)-H_{\mathrm{MLC}}^{\mathrm{black}}\left(X_0,Y_0;A_{\mathrm{MLC}}^{\mathrm{black}}\right)}{H_{\mathrm{jaw}}\left(0,0;10\times 10_{\mathrm{iso}}\right)}\right]\cdot \mathrm{OCR}_{\mathrm{source}}\left(R_0\right)\cdot \mathrm{RRF}_{\mathrm{jaw}}\left(X_0,Y_0\right) \quad , \tag{23}$$

with $R_0=\sqrt{X_0^{\,2}+Y_0^{\,2}}$, where $\mathrm{OCR}_{\mathrm{source}}(R_0)$ is the source off-center ratio [6], obtained by assuming that it is a function of only for an open infinite A_{jaw} field (defined as the in-air beam intensity (in water collision kerma) at a point that is R_0 distant from the isocenter to that at the isocenter (that is, $\mathrm{OCR}_{\mathrm{source}}(0) = 1$), where the $\mathrm{OCR}_{\mathrm{source}}$ dataset was produced by applying an in-air chamber response function [4] of $y(R_0) = \exp(0.002R_0 - 0.00002R_0^2)$ to an in-air dose dataset measured only at points of $Y_{\mathrm{beam}} \geq 0$ on the Y_{beam} axis). $\mathrm{RRF}_{\mathrm{jaw}}$ is the jaw-collimator radiation reflection factor [6], letting $\mathrm{RRF}_{\mathrm{jaw}}$=1 and $\mathrm{RRF}_{\mathrm{jaw}}$>1, respectively, inside and outside the A_{jaw} field. For beams with no MLC device, we obtain $H_{\mathrm{MLC}}^{\mathrm{black}}$=0 by setting $A_{\mathrm{MLC}} = \infty$ (infinite field) and $A_{\mathrm{MLC}}^{\mathrm{black}}$ in equation 23 (see Appendix C for definitions of "off-center jaw-S_c factor", "MLC-S_c factor" and "jaw-S_c factor").

First, we formulate [6] H_{jaw} in equation 23 as

$$H_{\mathrm{jaw}}\left(X_0,Y_0;A_{\mathrm{jaw}}\right)=\left(1+a_1C_{\mathrm{jaw}}^{\mathrm{eq}}\right)\cdot\left[G_{\mathrm{jaw}}^{\mathrm{S}}\left(X_0,Y_0;A_{\mathrm{jaw}}\right)+a_2G_{\mathrm{jaw}}^{\mathrm{F}}\left(X_0,Y_0;A_{\mathrm{jaw}}\right)\right], \tag{24}$$

$$G_{\mathrm{jaw}}^{\mathrm{S}}\left(X_0,Y_0;A_{\mathrm{jaw}}\right)=\frac{1}{\pi(\lambda_{\mathrm{S}}/2)^2}\int_{U_{\mathrm{S}}}\exp\left[-R_{\mathrm{S}}^{\,2}/(\lambda_{\mathrm{S}}/2)^2\right]\mathrm{d}A_{\mathrm{S}}, \tag{25}$$

$$G_{\mathrm{jaw}}^{\mathrm{F}}\left(X_0,Y_0;A_{\mathrm{jaw}}\right)=\frac{1}{\pi(\lambda_{\mathrm{F}}/2)^2}\int_{U_{\mathrm{F}}}\exp\left[-R_{\mathrm{F}}^{\,2}/(\lambda_{\mathrm{F}}/2)^2\right]\mathrm{d}A_{\mathrm{F}}, \tag{26}$$

where $C_{\mathrm{jaw}}^{\mathrm{eq}}$ is the side of the equivalent square field for A_{jaw}; and a_1, a_2, λ_{S} and λ_{F} are constants, where it is assumed that a_1 (the monitor-backscatter coefficient) is influenced only by the jaw collimator, which forms the A_{jaw} field, and not by the MLC or by the wedge. For the present 10-MV X-ray accelerator, we have obtained a_1 = 0.00146 cm^{-1}, a_2 = 0.0830, λ_{S} = 0.299 cm and λ_{F} = 3.097 cm. It can be understood that H_{jaw} approaches zero as the A_{jaw} field approaches zero.

Next, we formulate [16] $H_{\mathrm{MLC}}^{\mathrm{black}}$ in equation 23 as

$$H_{\mathrm{MLC}}^{\mathrm{black}}\left(X_0,Y_0;A_{\mathrm{MLC}}^{\mathrm{black}}\right)=\left(1+a_1C_{\mathrm{jaw}}^{\mathrm{eq}}\right)\cdot\left[G_{\mathrm{MLC}}^{\mathrm{S}}\left(X_0,Y_0;A_{\mathrm{MLC}}^{\mathrm{black}}\right)+a_2G_{\mathrm{MLC}}^{\mathrm{F}}\left(X_0,Y_0;A_{\mathrm{MLC}}^{\mathrm{black}}\right)\right], \tag{27}$$

$$G_{\mathrm{MLC}}^{\mathrm{S}}\left(X_0,Y_0;A_{\mathrm{MLC}}^{\mathrm{black}}\right)=\frac{1}{\pi\left(\lambda_{\mathrm{S}}/2\right)^2}\int_{U_{\mathrm{S}}}\left[1-\Upsilon_{\mathrm{MLC}}\left(X_0^{\mathrm{MLC}},Y_0^{\mathrm{MLC}}\right)\right]\cdot\exp\left[-R_{\mathrm{S}}^{\,2}/\left(\lambda_{\mathrm{S}}/2\right)^2\right]\mathrm{d}A_{\mathrm{S}}, \tag{28}$$

$$G_{\mathrm{MLC}}^{\mathrm{F}}\left(X_0,Y_0;A_{\mathrm{MLC}}^{\mathrm{black}}\right)=\frac{1}{\pi\left(\lambda_{\mathrm{F}}/2\right)^2}\int_{U_{\mathrm{F}}}\left[1-\Upsilon_{\mathrm{MLC}}\left(X_0^{\mathrm{MLC}},Y_0^{\mathrm{MLC}}\right)\right]\cdot\exp\left[-R_{\mathrm{F}}^{\,2}/\left(\lambda_{\mathrm{F}}/2\right)^2\right]\mathrm{d}A_{\mathrm{F}}, \tag{29}$$

where point (X_0^{MLC}, Y_0^{MLC}) should be within the $A_{\mathrm{MLC}}^{\mathrm{black}}$ region (Figure 5a,b show how point Q, area element dA_{S} (or dA_{F}), point O_{S} and point (X_0^{MLC}, Y_0^{MLC}) are related); and Υ_{MLC} is the MLC attenuation factor, evaluated using the beam water collision kerma along the ray line connecting points O_{S} and X_0^{MLC}, Y_0^{MLC} as

$$\Upsilon_{\mathrm{MLC}}\left(X_0^{\mathrm{MLC}},Y_0^{\mathrm{MLC}}\right)=\frac{\sum_{N=1}^{N_{\max}}\left(\frac{\mu_{\mathrm{en}}(E_N)}{\rho}\right)_{\mathrm{water}}\cdot\Psi\left(E_N,R_0^{\mathrm{MLC}}\right)\cdot\exp\left[-\mu_{\mathrm{MLC}}\left(E_N\right)\cdot T_{\mathrm{MLC}}\left(X_0^{\mathrm{MLC}},Y_0^{\mathrm{MLC}}\right)\right]\Delta E_N}{\sum_{N=1}^{N_{\max}}\left(\frac{\mu_{\mathrm{en}}(E_N)}{\rho}\right)_{\mathrm{water}}\cdot\Psi\left(E_N,R_0^{\mathrm{MLC}}\right)\Delta E_N}, \tag{30}$$

with $R_0^{\mathrm{MLC}}=\sqrt{\left(X_0^{\mathrm{MLC}}\right)^2+\left(Y_0^{\mathrm{MLC}}\right)^2}$, where T_{MLC} is the MLC effective thickness measured along the ray line connecting points O_{S} and (X_0^{MLC}, Y_0^{MLC}) (it should be noted that we obtain Υ_{MLC} = 1 for T_{MLC} = 0); $(\mu_{\mathrm{en}}\ (E_N)/\rho)_{\mathrm{water}}$ is the mass energy absorption coefficient of water for E_N photons; and $\Psi\left(E_N,R_0^{\mathrm{MLC}}\right)$ expresses the energy fluence spectrum for an open infinite jaw field, as a function of the energy bin (E_{N}) and the off-axis distance (R_0= R_0^{MLC}) (Figure 7), normalized as $\sum_{N=1}^{N_{\max}}\Psi\left(E_N,R_0\right)\Delta E_N=1$.

If T_{MLC} =0 for all points on the isocenter plane, we have $H_{\mathrm{MLC}}^{\mathrm{black}}$ =0 (that is, no MLC setting for the A_{jaw} field). Ideally, Υ_{MLC} should be evaluated along the line connecting point Q and dA_{S} (or dA_{F}). However, we did not use this procedure, because, along such a line, the spectrum estimation has not yet been established, and calculation of the effective thickness of the MLC is very complicated.

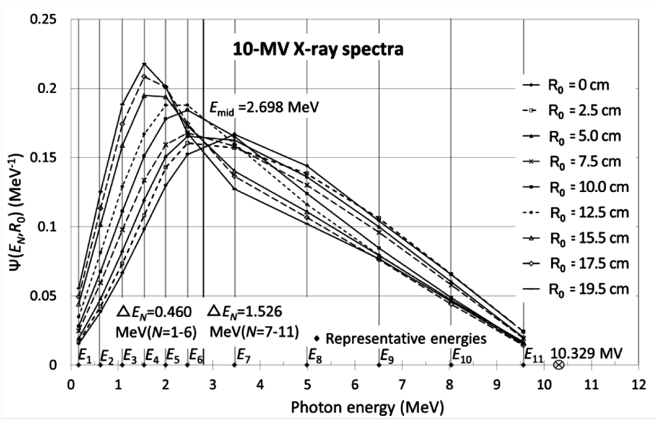

Figure 7 A normalized set of energy fluence spectra ($\Psi(E_N,R_0)$ (N = 1–11)) for 10-MV X-rays (with an accelerating voltage of 10.329 MV), reconstructed at off-axis distances of R_0 = 0, 2.5, 5.0, 7.5, 10.0, 12.5, 15.5, 17.5 and 19.5 cm. The energy bins are E_1=0.167 (= $E_{\min}$), E_2 = 0.627, E_3 = 1.087, E_4 = 1.548, E_5 = 2.008, E_6 = 2.468, E_7 = 3.461, E_8 = 4.987, E_9 = 6.513, E_{10} = 8.040 and E_{11} = 9.566 MeV (= $E_{\max}$) (namely, and E_{mid} = 2.698 MeV with ΔE_N = 0.460 MeV for N = 1–6, and with ΔE_N = 1.526 MeV for N = 7–11).

The total in-air energy fluence

For an open infinite jaw field yielding an in-air water collision kerma of $OCR_{source}(R_0)$ on the isocenter plane (equation 23), the total in-air energy fluence ($\Psi^{in\_air}_{total}$) at point (X_o, Y_o) can be evaluated as

$$\Psi^{in\_air}_{total}(X_0,Y_0)=\frac{OCR_{source}(R_0)}{\sum_{N=1}^{N_{max}}\left(\frac{\mu_{en}(E_N)}{\rho}\right)_{water}\cdot\Psi(E_N,R_0)\Delta E_N}, \qquad (31)$$

with $R_0=\sqrt{X_0^{\,2}+Y_0^{\,2}}$. It should be noted that the denominator of equation 31 expresses the total water collision kerma that the normalized energy fluence spectrum yields at the corresponding point in air. Therefore, the in-air energy fluence related to the normalized energy fluence of $\Psi(E_N,R_0)\Delta E_N$ yields the following in-air water collision kerma:

$$K^{in\_air}_{water}(R_0;E_N)=\Psi^{in\_air}_{total}(R_0)\cdot\left(\frac{\mu_{en}(E_N)}{\rho}\right)_{water}\cdot\Psi(E_N,R_0)\Delta E_N, \qquad (32)$$

The in-phantom dose calculations described below are carried out using the $K^{in\_air}_{water}$ function. If a wedge filters the open jaw or MLC field, we calculate the in-air water collision kerma variation for each set of primary photons (N = 1 to N_{max}), depending on the wedge thickness along the corresponding ray line. This is because the in-phantom dose is calculated by using the primary photons emitted from the source *(S)* and by treating the phantom, the wedge and the MLC as parts of a unified irradiation body.

Calculation K^{jaw}_{water} of and K^{MLC}_{water}

This section is described mainly by referring to figures 4, 5, 8, and 9, where the 2D wedge and MLC plates are placed at $Z_{beam} = Z_{wedge}$ and $Z_{beam} = Z_{MLC}$ respectively. We set up the precondition that the 2D wedge and MLC plates hold data regarding the thicknesses (or effective thicknesses) of the 3D wedge and the MLC devices, respectively, measured along the ray lines emanating from the source *(S)*. In the inserted diagram on the right in Figure 8, we let T_0 denote the thickness (or effective thickness) measured along a ray line passing through a point (X^L_U, Y^L_U, Z^L_U) on the wedge or MLC plate and through a point $Q(X_0, Y_0)$ on the isocenter plane, and let α_1 denote the angle between the ray line and the isocenter plane. Then the thickness (or effective thickness) along the line that is parallel to the Z_{beam} axis and passes through the point (X^L_U, Y^L_U, Z^L_U) can be approximated as $T_0 \sin\alpha_1$. Draw an axis *r'* from a dose calculation point $P(X_C, Y_C, Z_C)$ that passes through the point (X^L_U, Y^L_U, Z^L_U). Then the thickness (or effective thickness) measured along the *r'* axis can be approximated as $T_0 \sin\alpha_1/\sin\alpha_2$, where α_2 is the angle between the *r'* axis and the isocenter plane. On the basis of this procedure, the following describes how to handle the 3D wedge and MLC devices.

First, we refer to the thickness (or effective thickness) measured from the bottom side along the *r'* axis using the symbol U^L (L = 1 to L_{max}). The diagram shows the case when L_{max} = 5 with equal interval sections ΔL_0 and a residual section $\Delta L'_0$ ($\leq \Delta L_0$) along a line parallel to the Z_{beam} axis. We estimate the value for U^L as

$$U^L=(T_0-T^L_U)\sin\alpha_1/\sin\alpha_2, \qquad (33)$$

with

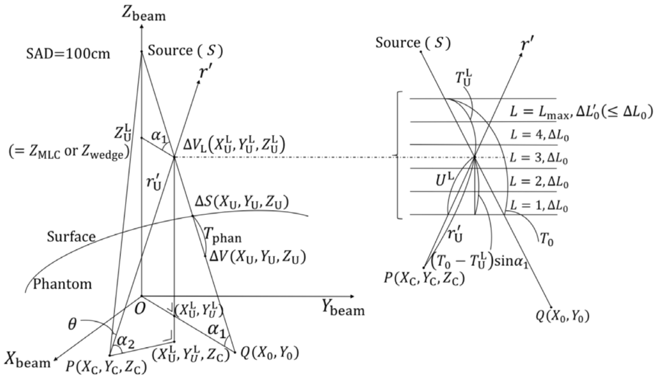

Figure 8 Diagrams showing how to calculate the thickness (U^L) of the wedge or MLC measured from the bottom side along the *r'* axis connecting a dose calculation point $P(X_C, Y_C, Z_C)$ and a point (X^L_U, Y^L_U, Z^L_U) in the wedge or MLC plate, and showing how to calculate the beam water collision kerma at a volume element (ΔV_L) in the wedge or MLC. Let T_0 be the thickness (or effective thickness) of the wedge or MLC, measured along the line connecting the source *(S)* and a point $Q(X_0, Y_0)$ on the isocenter plane. The inserted diagram on the right is for the case L_{max} = 5. The diagrams also assist in calculating the beam water collision kermas at an area element (ΔS) on the phantom surface and a volume element (ΔV) in the phantom, in relation to the wedge or MLC setting for the beam.

$$T^L_U=\left[(L_{max}-L-0.5)\Delta L_0+\Delta L'_0\right]/\sin\alpha_1,\ (L=1,2,\cdots,L_{max}-1), \qquad (34)$$

$$T^{L_{max}}_U=0.5\Delta L'_0/\sin\alpha_1, \qquad (35)$$

$$\sin\alpha_1=\left[(L_{max}-1)\Delta L_0+\Delta L'_0\right]/T_0, \qquad (36)$$

It should be noted that, at least for wedge filters, the calculation for U^L is a close approximation because they are constructed with continuously gentle slope faces against the isocenter plane.

Second, at the point (X^L_U, Y^L_U, Z^L_U) in the L^{th} section (Figures 8 and 9), we set an imaginary volume element (ΔV_L) that is surrounded both by the ΔL_0 or $\Delta L'_0$ layer faces and by the quadrangular pyramid faces determined by (r', θ, $\Delta\theta$, φ, $\Delta\varphi$) whose apex is located at point $P(X_C, Y_C, Z_C)$. Let ΔA_0 denote the area of the pyramid base at the point (X^L_U, Y^L_U, Z^L_U) perpendicular to the r' axis; r'_u denotes the distance between points $P(X_C, Y_C, Z_C)$ and (X^L_U, Y^L_U, Z^L_U); and θ'_u denotes the angle between the Z_{beam} axis (or the Z'_{beam} axis starting

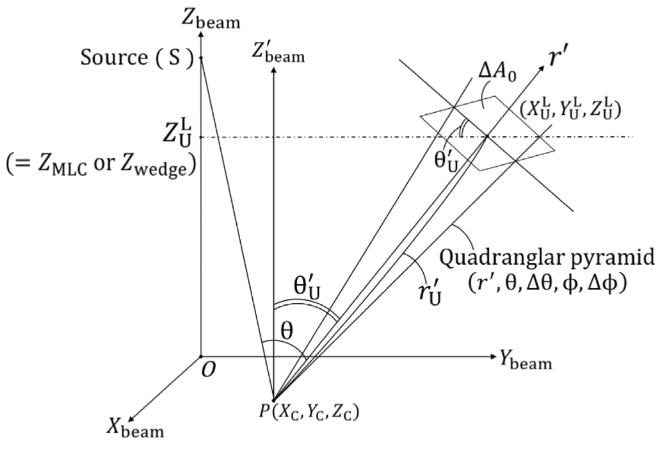

Figure 9 Diagram showing how to calculate the magnitude of the volume element (ΔV_L) in the L^{th} section, surrounded by both the ΔL_0 or $\Delta L'_0$ section faces and by the quadrangular pyramid faces determined by (r', θ, $\Delta\theta$, φ, $\Delta\varphi$) whose apex is located at point *P*. ΔA_0 denotes the area of the pyramid base at point (X^L_U, Y^L_U, Z^L_U), perpendicular to the r' axis, and θ'_u denotes the angle between the Z_{beam} (or Z'_{beam}) axis and the *r'* axis.

at point P and parallel to the Z_{beam} axis) and the r' axis. Then the magnitude of (ΔV_L) is given as

$$\Delta V_L = \frac{\Delta A_0 \Delta L_0}{\cos\theta_U'},\ (L = 1, 2, \cdots, L_{\max} - 1)\ , \tag{37}$$

$$\Delta V_{L_{\max}} = \Delta A_0 \Delta L_0' / \cos\theta_U'\ , \tag{38}$$

with

$$\Delta A_0 = r_U'^2 \left\{\cos(\theta - \Delta\theta/2) - \cos(\theta + \Delta\theta/2)\right\}\Delta\phi\ , \tag{39}$$

To calculate the primary and scatter doses from the wedge and MLC bodies, we used ΔL_0 = 0.01 cm and ΔL_0 = 0.1 cm, respectively. To calculate both the primary and scatter doses from the wedge holder, we used ΔL_0 = 0.2 cm (that is, $L_{\max}$ = 1 in Figure 8). The value of T_0 measured along each ray line was obtained by analyzing the manufacturer's diagrams. However, we assumed that each of the MLC leaves had no driving screw holes (0.33 cm and 0.43 cm in diameter for the 0.5 cm and 1 cm wide leaves, respectively).

Next, we describe the calculation of the beam water collision kermas of $K_{\text{water}}^{\text{MLC}}$ and $K_{\text{water}}^{\text{jaw}}$ (equations 1-3) for a given volume element (ΔV or ΔV_L) or a given area element ΔS within the unified irradiated body (Figure 8). Because the X-ray emission from the flattening filter is very small relative to that from the X-ray target (for the present 10-MV X-ray accelerator, the strength ratio of the extra radiation source to the X-ray target for an infinite A_{jaw} field is α_2 = 0.0830 (equation 24), we assumed that all X-rays emanate from the source *(S)*.

It has been found that, particularly under MLC field irradiation, the $\text{OPF}_{\text{in\_air}}$ factor (equation 23) determined on the basis of a single point within each ΔV element in the phantom cannot give accurate dose calculation results. This is mainly caused by the nonuniformity of the beam intensities within each ΔV element owing to the use of the MLC. In the following dose calculation procedures, the symbol $\text{OPF}_{\text{in\_air}}^{\text{single}}$ is used when the beam intensity for each ΔV element in the phantom should be evaluated based on the beam intensity at a single point within each ΔV element. On the other hand, the symbol $\text{OPF}_{\text{in\_air}}^{\text{multi}}$ is used when the in-air beam intensity for each ΔV element in the phantom should be evaluated based on the beam intensities at multiple points within each ΔV element (the details will be described later in equation 47).

Here we classify the wedge irradiation mode using wedge types = 0 to 4, stipulating that wedge type = 0 signifies irradiation with no wedge (that is, open jaw or MLC field irradiations), and wedge types 1, 2, 3 and 4 denote jaw or MLC field irradiations with the use of a 15°, 30°, 45° and 60° wedge, respectively. Under these conditions, the following (a)-(e) describe the evaluation of the beam intensity for a point (X_U^L, Y_U^L, Z_U^L) (L = 1 to $L_{\max}$) within the MLC or wedge, or for a point (X_U, Y_U, Z_U) on the phantom surface or within the phantom (Figure 8), these points are on a ray line passing through point Q(X_0, Y_0) on the isocenter plane).

(a) For the beam intensity calculation within the MLC device, we set $Z_U^L = Z_{\text{MLC}}$ (= 53.7 cm), which is determined by analyzing calculated and measured MLC-S_c datasets (Figure 6). The $K_{\text{water}}^{\text{jaw}}$ collision kerma caused by the E_N photons for the ΔV_L element at the point $\left(X_U^L, Y_U^L, Z_{\text{MLC}}\right)$ in the L^{th} section of the MLC plate should be evaluated only under a given A_{jaw} opening, because the MLC device is placed in close proximity to the jaw collimator; that is, an MLC field of A_{MLC} = ∞ should be used to evaluate $\text{OPF}_{\text{in\_air}}^{\text{single}}$ in the following equation. Therefore, the calculation is performed as follows:

$$K_{\text{water}}^{\text{jaw}}\left(X_U^L, Y_U^L, Z_{\text{MLC}}; E_N\right)_{\text{MLC}} = \Psi_{\text{total}}^{\text{in\_air}}\left(X_0, Y_0\right)\cdot \text{OPF}_{\text{in}_{\text{air}}}^{\text{single}}\left(X_0, Y_0; A_{\text{MLC}} = \infty, A_{\text{jaw}}\right)\cdot\left(\frac{\mu_{\text{en}}(E_N)}{\rho}\right)_{\text{water}}$$
$$\cdot\Psi\left(E_N, R_0\right)\Delta E_N\cdot\left(\frac{\text{SAD}}{\text{SAD} - Z_{\text{MLC}}}\right)^2\cdot\exp\left[-\mu_{\text{MLC}}\left(E_N\right)\cdot T_{\text{MLC}}^L\left(X_0, Y_0\right)\right]\ , \tag{40}$$

where SAD (= 100 cm) is the source–axis distance (or the distance between the source *(S)* and the isocenter plane); $T_{\text{MLC}}^L\left(X_0, Y_0\right)$ is the effective thickness of the MLC, measured along the corresponding ray line (Figure 8) from the MLC top side to the middle point $\left(X_U^L, Y_U^L, Z_{\text{MLC}}\right)$ of the L^{th} section; and $\mu_{\text{MLC}}(E_N)$ is the linear attenuation coefficient of the MLC material for E_N photons.

(b) For the beam intensity calculation within the wedge holder, we set $Z_U^L = Z_{\text{wedge}}$ (= 42.4 cm) with L = 1 (= $L_{\max}$; Figure 8). The $K_{\text{water}}^{\text{jaw}}$ collision kerma caused by the E_N photons for the ΔV_L element at the point $\left(X_U^L, Y_U^L, Z_{\text{wedge}}\right)$ in the L^{th} section of the wedge holder should also be evaluated only under a given A_{jaw} opening (that is, an MLC field of A_{MLC} = ∞ should be used for $\text{OPF}_{\text{in\_air}}^{\text{single}}$ in the following equation). Therefore, the calculation is performed as follows:

$$K_{\text{water}}^{\text{jaw}}\left(X_U^L, Y_U^L, Z_{\text{wedge}}; E_N\right)_{\text{w\_hold}} = \Psi_{\text{total}}^{\text{in\_air}}\left(X_0, Y_0\right)\cdot \text{OPF}_{\text{in\_air}}^{\text{single}}\left(X_0, Y_0; A_{\text{MLC}} = \infty, A_{\text{jaw}}\right)\cdot\left(\frac{\mu_{\text{en}}(E_N)}{\rho}\right)_{\text{water}}$$
$$\cdot\Psi\left(E_N, R_0\right)\Delta E_N\cdot\left(\frac{\text{SAD}}{\text{SAD} - Z_{\text{wedge}}}\right)^2\cdot\exp\left[-\left\{\mu_{\text{MLC}}\left(E_N\right)\cdot T_{\text{MLC}}\left(X_0, Y_0\right) + \mu_{\text{w\_hold}}\left(E_N\right)\cdot T_{\text{w\_hold}}^L\left(X_0, Y_0\right)\right\}\right]\ , \tag{41}$$

where $T_{\text{MLC}}(X_0, Y_0)$ is the thickness of the MLC, measured along the corresponding ray line (Figure 8); $T_{\text{w\_hold}}^L(X_0, Y_0)$ is the wedge-holder thickness (equation 35) measured along the corresponding ray line, from the wedge-holder top side to the middle point $\left(X_U^L, Y_U^L, Z_{\text{wedge}}\right)$ of the L^{th} section; and $\mu_{\text{w\_hold}}(E_N)$ is the linear attenuation coefficient of the wedge-holder material for the E_N photons. For the case of no MLC in the beam, we should set $T_{\text{MLC}}(X_0, Y_0) = 0$.

(c) For the beam intensity calculation within the wedge body, we set $Z_U^L = Z_{\text{wedge}}$ (= 42.4 cm) with L = 1, 2, ..., $L_{\max}$ (Figure 8). The $K_{\text{water}}^{\text{jaw}}$ collision kerma caused by the E_N photons for the element at the point $\left(X_U^L, Y_U^L, Z_{\text{wedge}}\right)$ in the L^{th} section of the wedge body should also be evaluated only under a given A_{jaw} opening (that is, A_{MLC} = ∞ should be used for $\text{OPF}_{\text{in\_air}}^{\text{single}}$ in the following equation). Therefore, the calculation is performed as follows:

$$K_{\text{water}}^{\text{jaw}}\left(X_U^L, Y_U^L, Z_{\text{wedge}}; E_N\right)_{\text{wedge}} = \Psi_{\text{total}}^{\text{in\_air}}\left(X_0, Y_0\right)\cdot \text{OPF}_{\text{in}_{\text{air}}}^{\text{single}}\left(X_0, Y_0; A_{\text{MLC}} = \infty, A_{\text{jaw}}\right)\cdot\left(\frac{\mu_{\text{en}}(E_N)}{\rho}\right)_{\text{water}}$$
$$\cdot\Psi\left(E_N, R_0\right)\Delta E_N\cdot\left(\frac{\text{SAD}}{\text{SAD} - Z_{\text{wedge}}}\right)^2\cdot\exp\left[-\left\{\mu_{\text{MLC}}\left(E_N\right)\cdot T_{\text{MLC}}\left(X_0, Y_0\right) + \mu_{\text{w\_hold}}\left(E_N\right)\cdot T_{\text{w\_hold}}^L(X_0, Y_0) + \mu_{\text{wedge}}\left(E_N\right)\cdot T_{\text{wedge}}^L(X_0, Y_0)\right\}\right]\ , \tag{42}$$

where T_{wedge}^L (X_0, Y_0) is the wedge-body thickness (equations 34 and 35) measured along the corresponding ray line, from the wedge-body top side to the middle point $\left(X_U^L, Y_U^L, Z_{\text{wedge}}\right)$ of the L^{th} section; and $\mu_{\text{wedge}}(E_N)$ is the linear attenuation coefficient of the wedge-body material for the E_N photons. For the case of no MLC in the beam, we should set $T_{\text{MLC}}(X_0, Y_0) = 0$.

(d) For the beam intensity calculation for the ΔS element at the point (X_U, Y_U, Z_U) on the phantom surface, we should take into account the A_{MLC} field under a given A_{jaw} opening. Under the condition that the wedge generally covers the beam, we let the K_{water}^{MLC} collision kerma for ΔS caused by E_N photons be calculated as follows:

$$K_{water}^{MLC}\left(X_U,Y_U,Z_U;E_N\right)_{phan\_\Delta S}=\Psi_{total}^{in\_air}\left(X_0,Y_0\right)\cdot OPF_{in\_air}^{single}$$
$$\left(X_0,Y_0;A_{MLC},A_{jaw}\right)\cdot CF_{OPF}^{a}\left(A_{MLC}^{in\_jaw}/A_{jaw};\text{wedge type}\right)$$
$$\cdot CF_{OPF}^{b}\left(T_{MLC}\left(X_0,Y_0\right);A_{MLC}^{in\_jaw}/A_{jaw}\right)\cdot\left(\frac{\mu_{en}\left(E_N\right)}{\rho}\right)_{water}\cdot\Psi\left(E_N,R_0\right)\Delta E_N\cdot\left(\frac{SAD}{SAD-Z_U}\right)^2$$
$$\cdot\exp\left[-\{\mu_{w\_hold}\left(E_N\right)\cdot T_{w\_hold}(X_0,Y_0)+\mu_{wedge}\left(E_N\right)\cdot T_{wedge}(X_0,Y_0)\}\right], \quad (43)$$

with

$$CF_{OPF}^{b}\left(T_{MLC}\left(X_0,Y_0\right);A_{MLC}^{in\_jaw}/A_{jaw}\right)=\exp\left[\eta_{MLC}\left(A_{MLC}^{in\_jaw}/A_{jaw}\right)\cdot T_{MLC}\left(X_0,Y_0\right)\right], \quad (44)$$

$$\eta_{MLC}\left(A_{MLC}^{in\_jaw}/A_{jaw}\right)=0.12\times\left(1-A_{MLC}^{in\_jaw}/A_{jaw}\right)^{0.5}, \quad (45)$$

where $A_{MLC}^{in\_jaw}$ is the field area that the MLC collimator forms inside the A_{jaw} field on the isocenter plane (that is, $0\le A_{MLC}^{in\_jaw}/A_{jaw}\le 1$); $T_{MLC}(X_0, Y_0)$ is the effective thickness of the MLC, measured along the corresponding ray line (note that, for any ray line within the MLC field, we should set $T_{MLC}(X_0, Y_0) = 0$); CF_{OPF}^{a} is a factor introduced to make a small correction for the beam intensity calculation by employing $OPF_{in\_air}^{single}$, given as a function of both $A_{MLC}^{in\_jaw}/A_{jaw}$, and the wedge type (Appendix D); CF_{OPF}^{b} is a factor introduced to correct for the beam intensity calculation, given as a function of $T_{MLC}(X_0, Y_0)$ and $A_{MLC}^{in\_jaw}/A_{jaw}$, finely adjusting the degree of X-ray penetration when passing through the MLC effective thickness of $T_{MLC}(X_0, Y_0)$ along the corresponding ray line; and $T_{w\_hold}(X_0, Y_0)$ and $T_{wedge}(X_0, Y_0)$ are the thicknesses of the wedge holder and the wedge body, respectively, measured along the ray line (for the case of no wedge device in the beam, we should set $T_{w\_hold}(X_0, Y_0) = T_{wedge}(X_0, Y_0) = 0$.

(e) To calculate the beam intensity for the ΔV element at the point (X_U, Y_U, Z_U) within the phantom, we should also take into account the A_{MLC} field under a given A_{jaw} opening. Here, it should be noted that the ray line passing through the point (X_0, Y_0) on the isocenter plane should also pass through the effective point (Figure 2b) within the ΔV element. It has been found that the same CF_{OPF}^{a} and CF_{OPF}^{b} factors as before should be used to make small corrections also for the beam intensity calculation by employing $OPF_{in\_air}^{multi}$. Assuming that the wedge generally covers the beam, we let the K_{water}^{MLC} collision kerma for ΔV caused by the E_N photons are calculated as follows:

$$K_{water}^{MLC}\left(X_U,Y_U,Z_U;E_N\right)_{phan\_\Delta V}=\Psi_{total}^{in\_air}\left(X_0,Y_0\right)\cdot OPF_{in\_air}^{multi}\left(X_0,Y_0;A_{MLC},A_{jaw};\text{wedge type}\right)$$
$$\cdot CF_{OPF}^{a}\left(A_{MLC}^{in\_jaw}/A_{jaw};\text{wedge type}\right)\cdot CF_{OPF}^{b}\left(X_0,Y_0;A_{MLC}^{in\_jaw}/A_{jaw}\right)\cdot$$
$$\left(\frac{\mu_{en}\left(E_N\right)}{\rho}\right)_{water}\cdot\Psi\left(E_N,R_0\right)\Delta E_N\left(\frac{SAD}{SAD-Z_U}\right)^2$$
$$\cdot\exp\left[-\left\{\mu_{w\_hold}\left(E_N\right)\cdot T_{w\_hold}\left(X_0,Y_0\right)+\mu_{wedge}\left(E_N\right)\cdot\right.\right.$$
$$\left.\left.T_{wedge}\left(X_0,Y_0\right)+\mu_{water}\left(E_N\right)\cdot T_{phan}\left(X_0,Y_0\right)\right\}\right], \quad (46)$$

where, assuming that the phantom is constructed of water-equivalent media, $T_{phan}(X_0, Y_0)$ is the effective thickness of the phantom, measured along the ray line from the phantom surface to the point (X_U, Y_U, Z_U) and $\mu_{water}(E_N)$ is the linear attenuation coefficient of water for the E_N photons. For the case of no wedge device in the beam, we should set $T_{w\_hold}(X_0, Y_0) = T_{wedge}(X_0, Y_0) = 0$. The $OPF_{in\_air}^{multi}$ factor is experimentally constructed as

$$OPF_{in\_air}^{multi}\left(X_0,Y_0;A_{MLC},A_{jaw};\text{wedge type}\right)$$
$$=\overline{OPF}\cdot\exp\left[-\lambda_{OPF}(A_{MLC}^{in\_jaw}/A_{jaw};\text{wedge type})\cdot W_{OPF}^{1.5}\right], \quad (47)$$

with

$$\lambda_{OPF}\left(A_{MLC}^{in\_jaw}/A_{jaw};\text{wedge type}\right)=\lambda_0(\text{wedge type})\cdot(1-A_{MLC}^{in\_jaw}/A_{jaw}), \quad (48)$$

$$\overline{OPF}=\left[\sum_{J=1}^{J_{max}}OPF_J\right]/J_{max}, \quad (49)$$

$$W_{OPF}=\left[\sqrt{\sum_{J=1}^{J_{max}}(OPF_J-\overline{OPF})^2/J_{max}}\right]/\overline{OPF}, \quad (50)$$

where λ_0= 1.25 (no units) for the irradiation mode of wedge type = 0 (that is, for open jaw and MLC fields), and λ_0 = 3.50 for the irradiation modes of wedge type =1-4 (that is, for wedge-filtered jaw and MLC fields). These λ_0 values were obtained by comparing the calculated and measured percentage depth dose (PDD) and off-center ratio (OCR) datasets. This paper uses J_{max} = 27 as the number of multiple points set within each ΔV element, through which ray lines of J = 1, 2,..., J_{max} pass (nine points on each of the three planes set perpendicular to the r' axis (Figure 2b); and OPF_J is the OPF_{in_air} factor (equation 23) at the point where the J ray line intersects the isocenter plane (Figure 2b). We have λ_{OPF} = 0 for $A_{MLC}^{in\_jaw}/A_{jaw}$ = 1 for any wedge type. W_{OPF} expresses the degree of nonuniformity of the incident beam intensity for a given ΔV element, determined by A_{jaw}, A_{MLC} and wedge type. It should be noted that, in equation 47, we generally have $OPF_{in\_air}^{multi}\le\overline{OPF}$. It has been found that the work of the $OPF_{in\_air}^{multi}$ factor becomes remarkable as the width of an MLC leaf-blocked section in a jaw field becomes narrow (Figures 10 and 11).

Spectra and dose kernels

We reconstructed [3, 4] a new set of energy fluence spectra for the accelerator as follows. We measured sets of in-air transmission data at points on the Y_{beam} axis where $Y_{beam}\ge 0$ using an ionization chamber with an acrylic buildup cap (a factor of f_{cap} = 0.25 was assumed [4] to account for radiation attenuation and scatter in the buildup cap), in which we used acrylic attenuators of 0–30 cm in thickness and lead attenuators of 0-3 cm in thickness at off-axis distances of R_0 = 0, 2.5, 5.0, 7.5, 10.0, 12.5, 15.5, 17.5 and 19.5 cm. We set a value of 10.329 MV for the accelerating voltage. Using a common set of energy bins for all the off-axis distances, we reconstructed a set of $\Psi(E_N,R_0)$ spectra with an accuracy of approximately ±1% for the measured transmission data. The energy bins were E_1 = 0.167 (= E_{min}), E_2 = 0.627, E_3 = 1.087, E_4 = 1.548, E_5 = 2.008, E_6 = 2.468, E_7 = 3.461, E_8 = 4.987, E_9 = 6.513, E_{10} = 8.040 and E_{11} = 9.566 MeV (= E_{max}) (namely, N_{max} = 11 and E_{mid} = 2.698 MeV with ΔE_N = 0.460 MeV for N = 1–6, and with ΔE_N = 1.526 MeV for N = 7–11). Figure 7 shows the reconstructed spectra at R_0 = 0-19.5 cm. The X-ray spectrum becomes softer as the off-axis distance (R_0) increases.

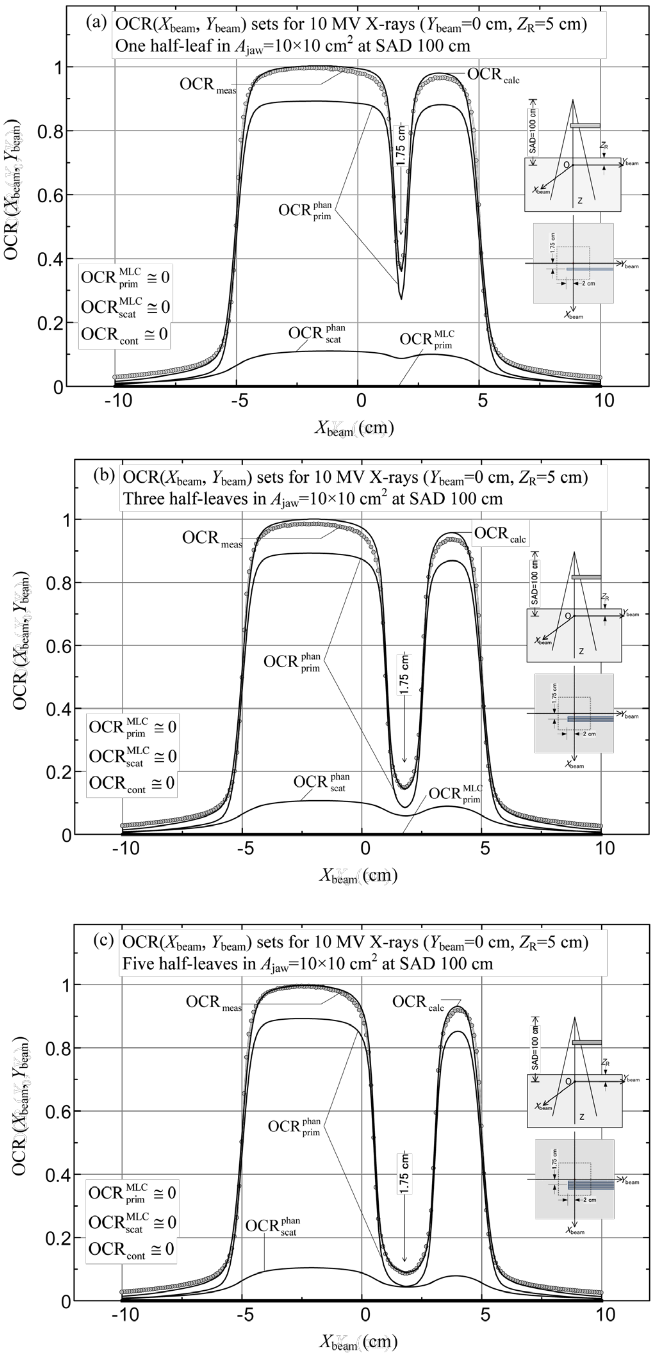

Figure 10 Graphs of the OCR_{calc} (including its components) and OCR_{meas} (in points) datasets, with the X_{beam} value varied with Y_{beam}= 0 cm on the isocenter plane at a reference depth of Z_R = 5 cm with no wedge used, founded by setting (a) one half-leaf (0.5 cm in width), (b) three consecutive half-leaves (1.5 cm in width) and (c) five consecutive half-leaves (2.5 cm in width) in a jaw field of A_{jaw} = 10 × 10 cm^2. 10-MV X-rays, SAD = 100 cm (each reference dose was obtained at Z_R = 5 cm using the open A_{jaw} field).

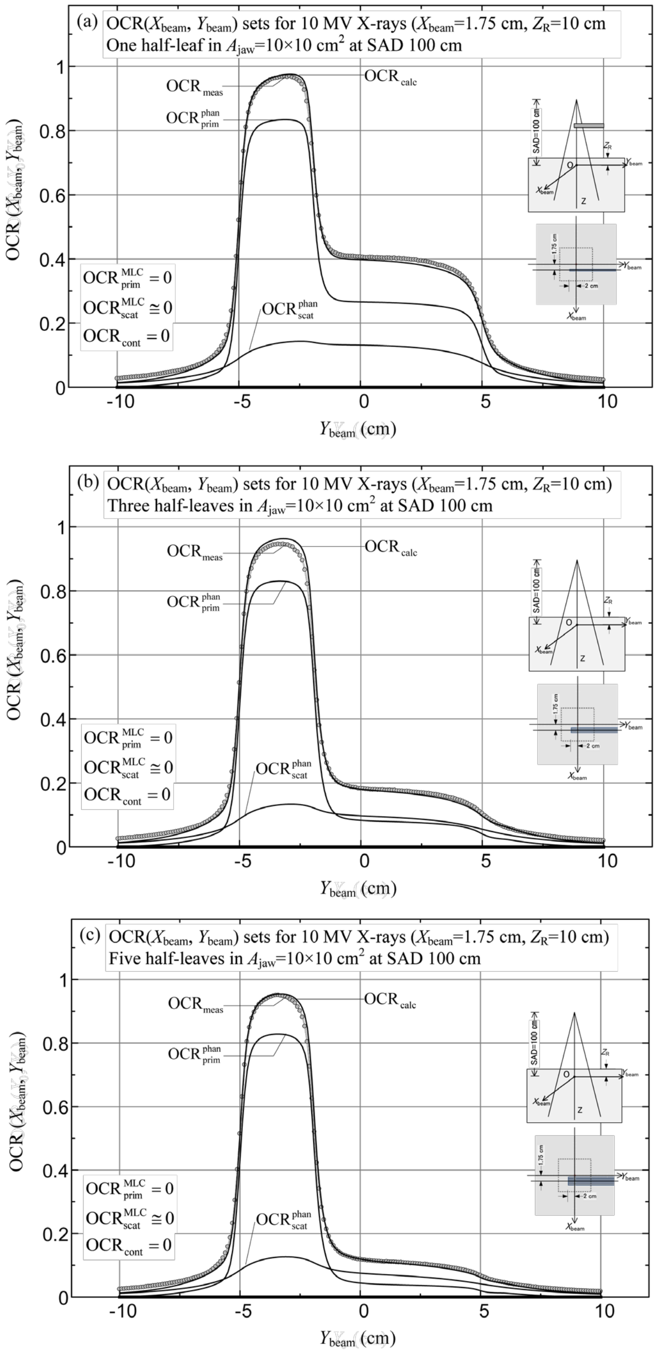

Figure 11 Graphs of the OCR_{calc} (including its components) and OCR_{meas} (in points) datasets, with the Y_{beam} value varied and X_{beam} = 1.75 cm on the isocenter plane at a reference depth of Z_R = 10 cm with no wedge used, founded by setting an MLC leaf-blocked section in a jaw field of A_{jaw} = 10 × 10 cm^2 with (a) one half-leaf (0.5 cm in width), (b) three consecutive half-leaves (1.5 cm in width) and (c) five consecutive half-leaves (2.5 cm in width). 10-MV X-rays, SAD = 100 cm (each reference dose was obtained at Z_R = 10 cm using the open A_{jaw} field).

$H_{1,2}$ and $K_{1,2}$ dose kernels

Primary and scatter dose kernels in water ($H_{1,2}$ and $K_{1,2}$) for the energy bins of E_N (N = 1 to 11) were produced through use of an Electron Gamma Shower (EGS) Monte Carlo code taking semi-infinite water phantoms (Figure A1). The primary and scatter dose kernels (as shown in Kimura and colleagues [7]) were produced, assuming the density of water to be unity.

Structure of the MLC

The MLC is made of a proprietary tungsten alloy. Accordingly, as an effective approach, we calculated the in-air output factor (OPF_{in_air}) for an open MLC field using equation 23 by assuming that the MLC was composed of tungsten atoms; however, its density was different from that of pure tungsten metal. We let the ratio of the mass density of the MLC material to that of the pure tungsten material be ρ_{MLC_factor} = 0.897 This ratio was obtained by comparing calculated and measured MLC-S_c datasets (Figure 6), which we calculated by setting a virtual 2D MLC plate at a distance of Z_{MLC} = 53.7 cm above the isocenter plane (Figure 4). On the whole, these numerical values gave the most accurate results for the MLC-S_c factor.

The MLC device is composed of sixty pairs of leaves. Let N^{leaf} denote the leaf number. At N^{leaf} = 1 and N^{leaf} = 60, each of the leaves forms a special shadow field 1.4 cm wide on the isocenter plane. At N^{leaf} = 2-10 and N^{leaf} = 51-59, each of the leaves forms a shadow field 1 cm wide, called a "full leaf" or "type 0." At N^{leaf} = 11-50 forms a shadow field 0.5 cm wide, called a "half leaf." The half leaves are classified into two types, type 1 and type 2, and these types are arrayed alternately. The full and half leaves have [23] a staple, a hook, a curved end, stepped sides and chamfers at both corners of the curved end so that these leaves can be moved to create an irregular field shape.

We analyzed the fine 3D structure of the full and half leaves as per the manufacturer's information. When the full and half leaves are consecutively arrayed, the isocenter-axis components of the MLC effective thicknesses calculated along the ray lines are separated into seven or eight sections, respectively, in the direction of the X_{beam}-axis (excluding the region around each curved end and ignoring the presence of the driving screw holes). Figure 12 illustrates the sectional widths measured on the isocenter plane for leaves of (a) type 0 (full), (b) type 1 (half) and (c) type 2 (half). The width of the region overlapped with the neighboring leaf is 0.067 cm; accordingly, each type has an actual width of 0.567 or 1.067 cm. The data in brackets give the isocenter-axis components. Figure 13 illustrates the 3D shapes of the isocenter-axis components for a single full or half leaf: (a) full leaf (type 0; using N^{leaf} = 10), (b) half leaf (type 1; using N^{leaf} = 30) and (c) half leaf (type 2; using N^{leaf} = 31). Note that the diagrams are drawn by setting the position of each leaf end at Y_{beam} = 0 cm.

MLC-S_c calculation

Using equation 23, we calculated the in-air output factor (OPF_{in_air}) under a given set of A_{MLC} and A_{jaw} fields along each center line of the seven or eight stripes using its sectional width (Figure 12) for each of the full or half MLC leaves. However, for N^{leaf} = 1 and 60 we assumed that each leaf had an infinite width, repeating the eight-striped pattern of the full leaf (to take into account the overrun area, as indicated by the circle in Figure 5b, when the X_{beam}-axis side edge of the A_{jaw} field is nearly equal to ±20 cm). Moreover, to effectively calculate near the leaf end, we used a series of ΔT^{leaf} steps on the middle line of each stripe, starting at the leaf end, as follows:

$$\Delta T_i^{leaf} = \Delta T_{min}^{leaf} + \frac{\left(\Delta T_{max}^{leaf} - \Delta T_{min}^{leaf}\right)}{2}\left[1-\cos\left\{\pi\left(1-\exp\left(-\frac{\ln 2}{T_H^{leaf}}T_{i-1}^{leaf}\right)\right)\right\}\right], \quad (51)$$

for $i = 1, 2, 3, \ldots$, where we let $T_0^{leaf} = 0$ cm and $T_i^{leaf} = T_{i-1}^{leaf} + \Delta T_i^{leaf}$. Then, we have $T_1^{leaf} = \Delta T_{min}^{leaf}$ and $T_\infty^{leaf} = \Delta T_{max}^{leaf}$ (the step increases slowly at small and large values of i). For the experimental studies, we used ΔT_{min}^{leaf}=0.01 cm, ΔT_{max}^{leaf} = 0.5 cm and T_H^{leaf}= 1.0187 cm.

Figure 6 shows the calculated and measured MLC-S_c datasets that were obtained at the isocenter ($X_0 = Y_0 = 0$ cm) as a function of the square A_{MLC} field side under each of the square A_{jaw} fields of 6 × 6 to 28 × 28 cm^2 in size (equation C2 in Appendix C), letting both A_{mlc} and A_{jaw} fields be symmetric with respect to the X_{beam} and Y_{beam} axes, and letting the other pairs of A and B MLC leaves be closed at Y_{beam}= 0 cm. The measurement was performed using a cylindrical mini-phantom [24] with a 0.6 cm^3 chamber (PTW 30006 Waterproof Farmer Chamber, Radiation Products Design, Inc. Albertville MN, USA) in free air. It can be seen that the measurement, having small waveforms for each of the

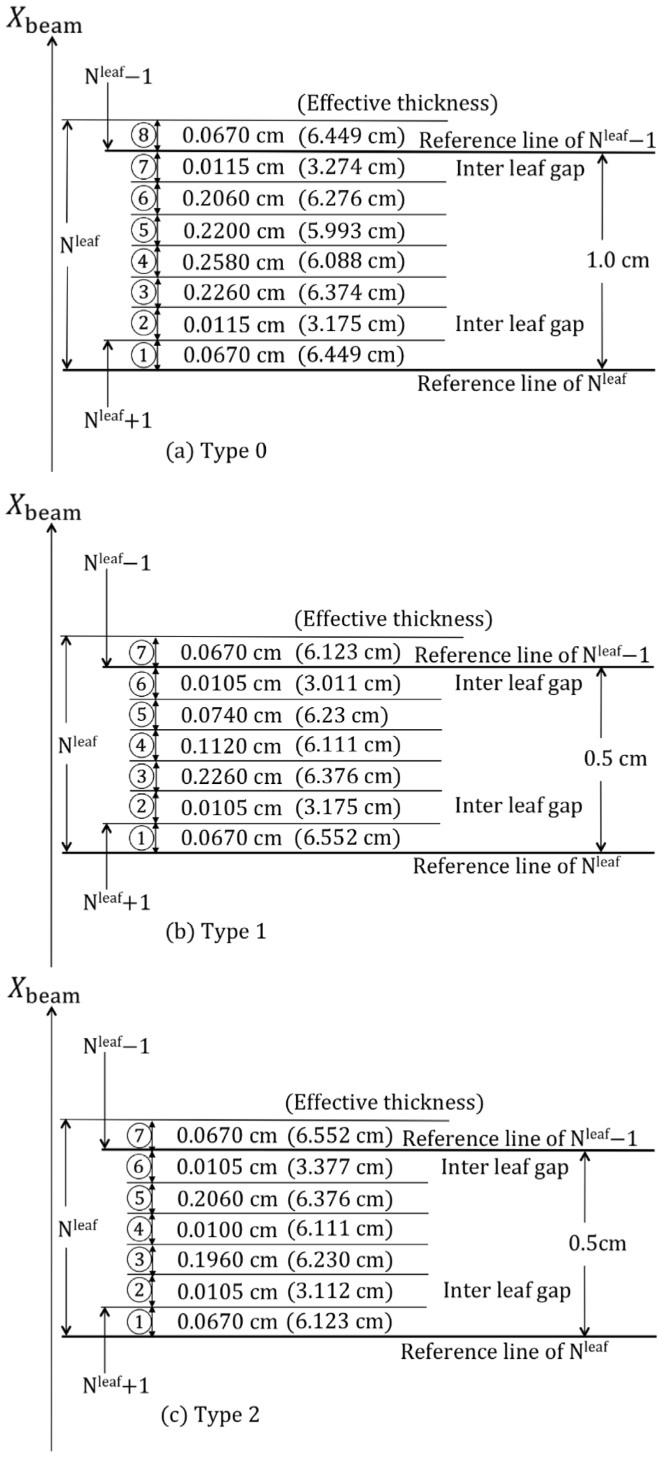

Figure 12 Sectional widths measured on the isocenter plane for leaves of (a) type 0 (full), (b) type 1 (half) and (c) type 2 (half). Each type has an actual width of 0.567 or 1.067 cm. Data in brackets show the isocenter-axis components of the MLC effective thicknesses measured along ray lines when the full or half leaves are continuously arrayed, excluding the region around each curved end and ignoring the presence of the driving screw hole.

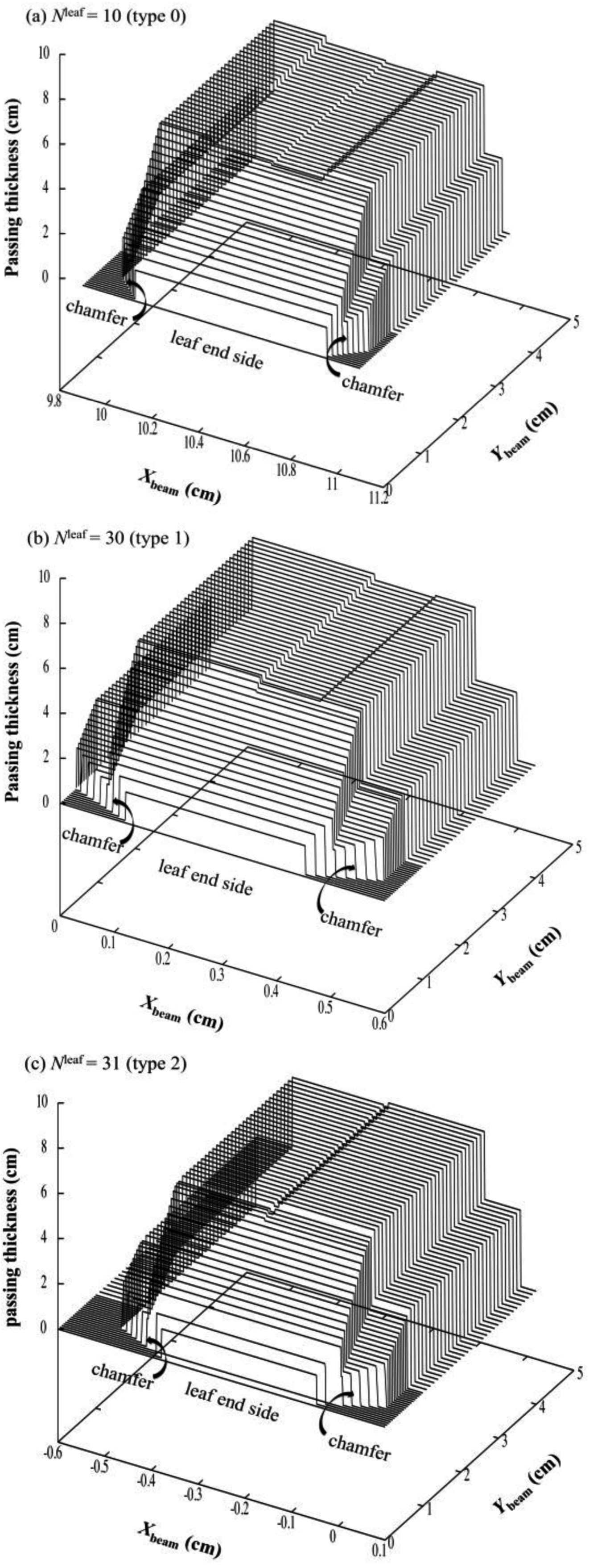

Figure 13 The 3D shapes of the isocenter-axis components of the MLC effective thicknesses calculated along ray lines, as a function of X_{beam} and Y_{beam}, for a single full or half leaf whose leaf end point is at Y_{beam}=0 cm (ignoring the presence of the driving screw hole): (a) for the full leaf (type 0; using N^{leaf} = 10), (b) for the half leaf (type 1; using N^{leaf} = 30) and (c) for the half leaf (type 2; using N^{leaf} = 31).

A_{jaw} fields, seems to be influenced to a certain degree by scattered radiation from the MLC leaves.

The mean absolute deviation of the calculations is 0.21% (the minimum is -0.71% and the maximum is 0.68%). The MLC-S_c factor depends largely on the A_{jaw} field; however, under a given A_{jaw} field, the MLC-S_c factor rapidly decreases from a certain A_{MLC} field size as the A_{MLC} field becomes smaller. It should be noted that, when the positions of the pairs of closed leaves are set at Y_{beam} = ±30 cm, the mean absolute deviation of the calculations is 0.22% (the minimum is -0.77% and the maximum is 0.67%). Therefore, it is clear that the in-air output factor (OPF_{in_air}) is influenced by the shapes of the MLC leaf structures. This is because the value of A_{MLC}^{black} calculated by setting the positions of the closed leaves at Y_{beam} = ±30 cm is greater than that calculated with Y_{beam}= 0 cm.

Structure of the wedge filters

The 15° and 30° wedge filters are made of proprietary iron alloys, and the 45° and 60° wedge filters are made of proprietary lead alloys. Accordingly, to effectively calculate the wedge-filtered dose, we introduced a factor, called ρ_{wedge_factor}, giving the ratio of the mass density of the wedge material to that of pure iron or lead (assuming, to a first approximation, that the wedge material is composed of iron or lead, though its density is different from the density of pure iron or lead) for each of the four wedges. We set ρ_{wedge_factor} = 0.900 for the 15° wedge; ρ_{wedge_factor} = 0.915 for the 30° wedge; ρ_{wedge_factor} = 0.955 for the 45° wedge; and ρ_{wedge_factor} = 0.930 for the 60° wedge. These factors were obtained by comparing calculated and measured PDD and OCR datasets.

Each wedge body is attached to a 0.2 cm thick acrylic plate. Figure 14 shows cross-sectional body views of the wedges. The vertical axis shows the isocenter-axis components of the wedge thickness measured along ray lines, as a function of X_{beam} or Y_{beam} on the isocenter plane. Each view forms a polygonal structure with corners marked by dots.

Calculation of PDD and OCR

The dose calculations in water phantoms described below were performed by setting the density of water to 0.990 g/cm^3 to obtain the most accurate calculation results (this value is approximately 0.65% less than that at room temperature). We calculated the dose at a point $P(X_C, Y_C, Z_C)$ in a water phantom, using a polar coordinate system (r', φ, θ) derived from the (x_v, y_v, z_v) coordinate system (Figure 2). Using the procedures described in Appendix B for setting steps of (Δr', Δφ, Δθ) and for setting the effective point for each volume element ΔV on the r'-axis, the dose calculation ability was assessed with PDD and OCR datasets that were measured in water phantoms using a 0.125 cm^3 ionization chamber (dimension of sensitive volume: radius 2.75 mm, length 6.5 mm; PTW 31002, Radiation Products Design, Inc.), setting the effective center of the chamber to coincide with each measuring point.

Setting the source–surface distance (SSD) to be 100 cm (equal to the source–axis distance (SAD)), we let the PDD be defined along the isocenter axis (X_{beam} = Y_{beam}= 0 cm) as:

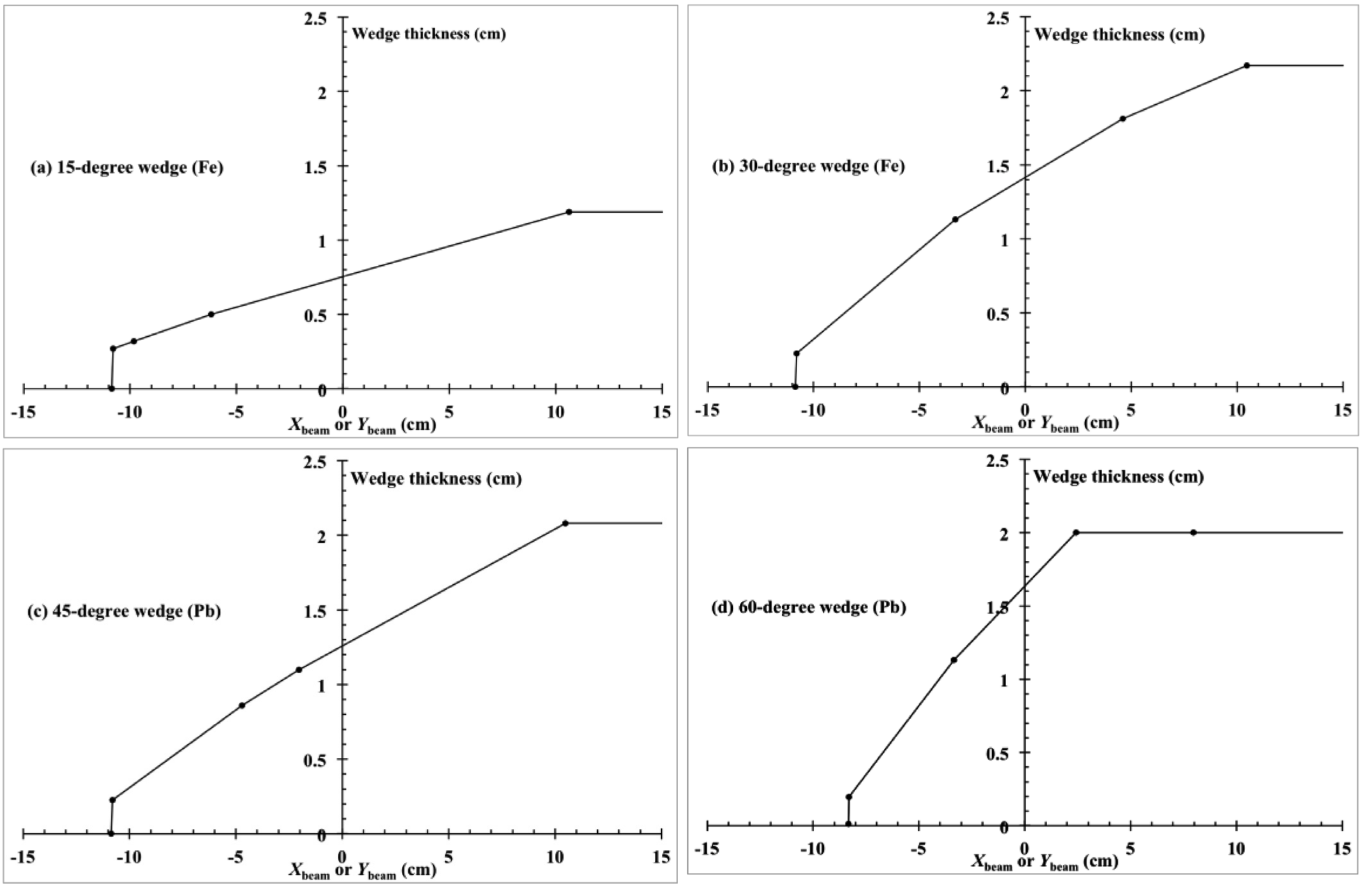

Figure 14 Cross-sectional body views of (a) the 15° wedge (steel alloy), (b) the 30° wedge (steel alloy), (c) the 45° wedge (lead alloy) and (d) the 60° wedge (lead alloy). The vertical axis shows the isocenter-axis components of the wedge thickness measured along ray lines, as a function of X_{beam} or Y_{beam}.

$$\mathrm{PDD}(Z) = 100 \times D_1(Z; A_{MLC}, A_{jaw}; \text{wedge type}) / D_1(Z_R; A^R_{MLC}, A^R_{jaw}; \text{wedge type}_R), \quad (52)$$

where D_1 in the numerator is the dose at a phantom at depth Z on the isocenter axis for an MLC field (A_{MLC}) under a jaw field (A_{jaw}) with no wedge used (wedge type = 0) or with one of the four wedges (wedge type = 1-4, also indicating its insertion direction); and D_1 in the denominator is the reference dose at a phantom at a reference depth of Z_R = 10 cm on the isocenter axis under a reference jaw field of $A^R_{jaw} = A_{jaw}$ with no MLC (namely, $A^R_{MLC} = \infty$, an infinite field) and with no wedge (wedge type$_R$ = 0), where the symbol D^R_1 is used below as the reference dose.

Next, setting the source–chamber distance (SCD) to be 100 cm (= SAD), we let the OCR be defined at a point (X_{beam}, Y_{beam}) on the isocenter plane (Z_{beam}= 0 cm) as:

$$\mathrm{OCR}(X_{beam}, Y_{beam}) = D_2(X_{beam}, Y_{beam}; A_{MLC}, A_{jaw}; Z_R; \text{wedge type}) / D_2(0,0; A^R_{MLC}, A^R_{jaw}; Z_R; \text{wedge type}_R) \quad (53)$$

where D_2 in the numerator is the dose at a point (X_{beam}, Y_{beam}) on the isocenter plane at a reference depth of Z_R on the isocenter axis for an MLC field (A_{MLC}) under a jaw field (A_{jaw}) with no wedge filter (wedge type = 0) or with one of the four wedges (wedge type = 1-4) also indicating its insertion direction); and D_2 in the denominator is the reference dose at the isocenter point on the isocenter plane at the reference depth (Z_R) under a reference jaw field of $A^R_{jaw} = A_{jaw}$ with no MLC (namely, $A^R_{MLC} = \infty$ and with no wedge (wedge type$_R$ = 0), where the symbol D^R_2 is used below as the reference dose.

According to the section of *Dose calculation principle*, each of D_1 and D_2 in equations 52 and 53 is typically composed of the nine dose components (D^{phan}_{prim}, D^{phan}_{scat}, D^{wedge}_{prim}, D^{wedge}_{scat}, $D^{w\_hold}_{prim}$, $D^{w\_hold}_{scat}$, D^{MLC}_{prim}, D^{MLC}_{scat} and D_{cont}) or the three dose components (D_{prim}, D_{scat} and D_{cont}).

Experimental studies and discussion

The PDD and OCR datasets in the water phantoms were calculated and measured, where the square A_{MLC} and A_{jaw} fields used below were all symmetric with respect to the X_{beam} and Y_{beam} axes. It should be noted that, for any given square field, the MLC leaves not taking part in forming the open A_{MLC} field were intentionally closed at Y_{beam}= 0 cm, and that each of the measured PDD or OCR datasets (drawn in dots in the figures below), producing the ratio of the dose relative to the reference dose, had a relative error of approximately ±0.7% because each measurement of D_1 and D_2 at a fixed point had a relative error of approximately ±0.5%.

PDD datasets

The calculated and measured PDD ($\mathrm{PDD_{calc}}$ and $\mathrm{PDD_{meas}}$) datasets, given as a function of the depth (Z) of a phantom on the isocenter axis under each irradiation condition, are shown below. Let the $\mathrm{PDD_{calc}}$ components corresponding to the nine dose components mentioned above be expressed as:

$$\mathrm{PDD}_{\mathrm{prim}}^{\mathrm{phan}} = 100 \times D_{\mathrm{prim}}^{\mathrm{phan}} / D_1^{\mathrm{R}}; \mathrm{PDD}_{\mathrm{scat}}^{\mathrm{phan}} = 100 \times D_{\mathrm{scat}}^{\mathrm{phan}} / D_1^{\mathrm{R}}; \mathrm{PDD}_{\mathrm{prim}}^{\mathrm{wedge}} = 100 \times D_{\mathrm{prim}}^{\mathrm{wedge}} / D_1^{\mathrm{R}};$$

$$\mathrm{PDD}_{\mathrm{scat}}^{\mathrm{wedge}} = 100 \times D_{\mathrm{scat}}^{\mathrm{wedge}} / D_1^{\mathrm{R}}; \mathrm{PDD}_{\mathrm{prim}}^{\mathrm{w\_hold}} = 100 \times D_{\mathrm{prim}}^{\mathrm{w\_hold}} / D_1^{\mathrm{R}}; \mathrm{PDD}_{\mathrm{scat}}^{\mathrm{w\_hold}} = 100 \times D_{\mathrm{scat}}^{\mathrm{w\_hold}} / D_1^{\mathrm{R}};$$

$$\mathrm{PDD}_{\mathrm{prim}}^{\mathrm{MLC}} = 100 \times D_{\mathrm{prim}}^{\mathrm{MLC}} / D_1^{\mathrm{R}}; \mathrm{PDD}_{\mathrm{scat}}^{\mathrm{MLC}} = 100 \times D_{\mathrm{scat}}^{\mathrm{MLC}} / D_1^{\mathrm{R}}; \text{and } \mathrm{PDD}_{\mathrm{cont}} = 100 \times D_{\mathrm{cont}} / D_1^{\mathrm{R}}$$

Then we have:

$$\mathrm{PDD}_{\mathrm{calc}} = \mathrm{PDD}_{\mathrm{prim}}^{\mathrm{phan}} + \mathrm{PDD}_{\mathrm{scat}}^{\mathrm{phan}} + \mathrm{PDD}_{\mathrm{prim}}^{\mathrm{wedge}} + \mathrm{PDD}_{\mathrm{scat}}^{\mathrm{wedge}} + \mathrm{PDD}_{\mathrm{prim}}^{\mathrm{w\_hold}} + \mathrm{PDD}_{\mathrm{scat}}^{\mathrm{w\_hold}} + \mathrm{PDD}_{\mathrm{prim}}^{\mathrm{MLC}} + \mathrm{PDD}_{\mathrm{scat}}^{\mathrm{MLC}} + \mathrm{PDD}_{\mathrm{cont}} \quad (54)$$

First, PDD(Z) datasets with no wedge used were calculated and measured for combinations of square A_{MLC} and A_{jaw} fields. We set MLC fields of A_{MLC} = 4 × 4-10 × 10 cm^2 for a jaw field of A_{jaw} = 10 × 10 cm^2; we set MLC fields of A_{MLC} = 4 × 4-15 × 15 cm^2 for a jaw field of A_{jaw} = 15 × 15 cm^2; and we set MLC fields of A_{MLC} = 4 × 4-20 × 20 cm^2 for a jaw field of A_{jaw} = 20 × 20 cm^2. Figures 15a-c show the PDD$_{\mathrm{calc}}$ (including its components) and PDD$_{\mathrm{meas}}$ datasets: diagram (a) is for a combination of A_{MLC} = 4 × 4 cm^2 and A_{jaw} = 10 × 10 cm^2 (details of the lower dose components are shown in diagram (b)); and diagram (c) is for a combination of A_{MLC} = 8 × 8 cm^2 and A_{jaw} = 10 × 10 cm^2 fields. It can be seen that (a) each of the primary and scatter doses from the MLC can be ignored; (b) the electron contamination dose decreases as the A_{MLC} field decreases for a given A_{jaw} field; and (c) the calculated data at depths greater than around 20 cm are approximately 1–2% greater than the corresponding measured data (this paper does not analyze further why such large deviations were produced); and (d) $\mathrm{PDD}_{\mathrm{prim}}^{\mathrm{MLC}}$ = 0 and PDD$_{\mathrm{cont}}$ = 0 at depths greater than approximately 5.8 cm. Results with almost the same calculation accuracy were also obtained for the other combinations of A_{MLC} and A_{jaw} fields.

Second, PDD(Z) datasets using the 15$^{\mathrm{o}}$, 30$^{\mathrm{o}}$, 45$^{\mathrm{o}}$ and 60$^{\mathrm{o}}$ wedges in the direction of the Y_{beam} axis were calculated and measured for combinations of square A_{MLC} and A_{jaw} fields as follows: we set A_{MLC} = 4 × 4 - 10 × 10 cm^2 for a jaw field of A_{jaw} = 10 × 10 cm^2; we set A_{MLC} = 4 × 4-15 × 15 cm^2 for a jaw field of A_{jaw} =15 × 15 cm^2; and we set A_{MLC} =4 × 4-20 × 20 cm^2 for a jaw field of A_{jaw} = 20 × 20 cm^2 (excluding the case where the 60$^{\mathrm{o}}$ wedge is used). Figure 16a-c show the PDD$_{\mathrm{calc}}$ (including its components) and PDD$_{\mathrm{meas}}$ datasets for a combination of A_{MLC} = 5 × 5 cm^2 and A_{jaw} = 15 × 15 cm^2 fields: diagram (a) is for the 15° wedge (details of the lower dose components are shown in diagram (b)); and diagram (c) is for the 60° wedge. It can be seen that the electron contamination dose virtually vanishes with the use of each of the wedges (namely, PDD$_{\mathrm{cont}}$ = 0), and that each of the primary and scatter doses from the wedge and MLC can be ignored (namely, $\mathrm{PDD}_{\mathrm{prim}}^{\mathrm{wedge}} \cong 0$ $\mathrm{PDD}_{\mathrm{scat}}^{\mathrm{wedge}} \cong 0$ $\mathrm{PDD}_{\mathrm{prim}}^{\mathrm{w_{hold}}} \cong 0$ $\mathrm{PDD}_{\mathrm{scat}}^{\mathrm{w\_hold}} \cong 0$ $\mathrm{PDD}_{\mathrm{prim}}^{\mathrm{MLC}} \cong 0$ $\mathrm{PDD}_{\mathrm{scat}}^{\mathrm{MLC}} \cong 0$ where $\mathrm{PDD}_{\mathrm{prim}}^{\mathrm{wedge}} = 0$ $\mathrm{PDD}_{\mathrm{prim}}^{\mathrm{w\_hold}} = 0$ and $\mathrm{PDD}_{\mathrm{prim}}^{\mathrm{MLC}} = 0$ at depths greater than approximately 5.6 cm). The calculation results in the buildup region are relatively poor (Figure 16a shows deviations = -28.2% (Z = 0.008 cm) to 6.8% (Z = 0.8 cm), and Figure 16c shows deviations = -80.7% (Z = 0.008 cm) to 8.2% (Z = 0.8 cm); this paper does not analyze further why such large deviations were produced), although the calculation results at depths beyond the buildup region are relatively accurate (Figure 16a shows deviations = -0.6% (Z = 10.2 cm) to 0.3% (Z = 2.6 cm), and Figure 16c shows deviations= -2% (Z = 30 cm) to 0.5% (Z = 2.5 cm). Results with almost the same calculation accuracy were also obtained for the other PDD datasets.

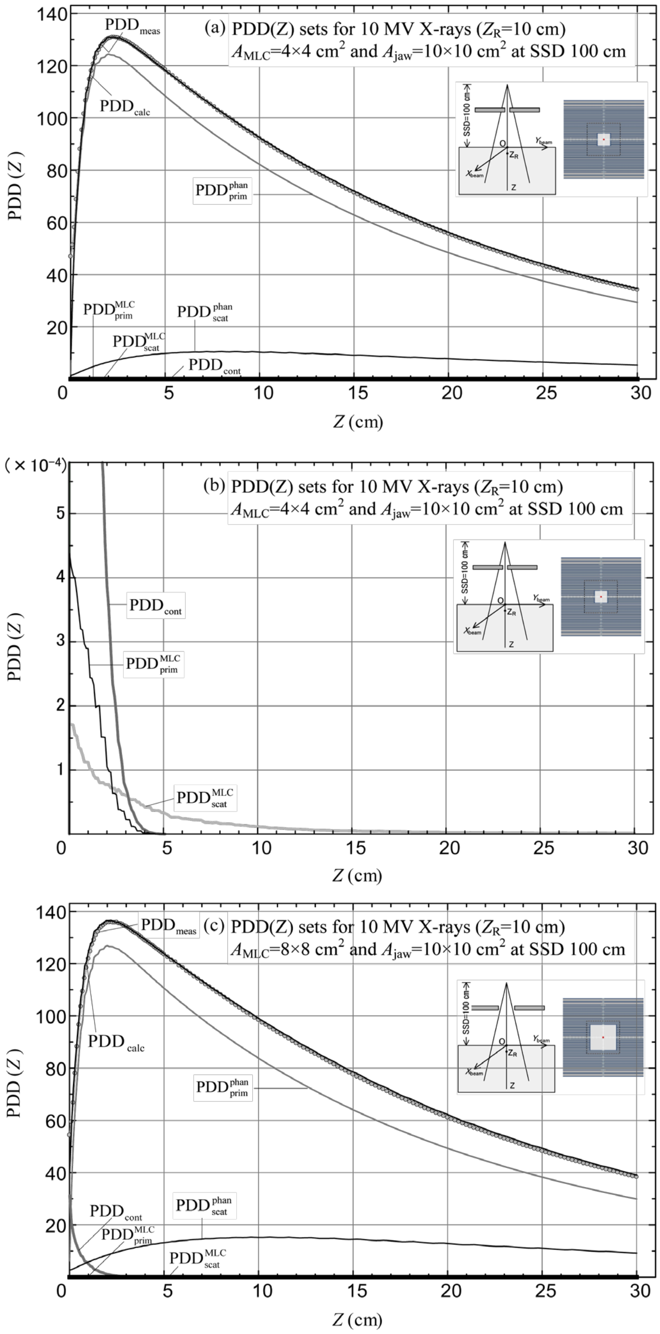

Figure 15 Graphs of the PDD$_{\mathrm{calc}}$ (including its components) and PDD$_{\mathrm{meas}}$ (in points) datasets in water with no wedge for (a) A_{MLC} = 4 × 4 cm^2 and A_{jaw} = 10 × 10 cm^2 (details of the lower dose region are shown in (b)) and for (c) A_{MLC} = 8 × 8 cm^2 and A_{jaw} = 10 × 10 cm^2. 10-MV X-rays, SSD=100 cm (each reference dose was obtained at Z_{R} = 10 cm using the open A_{jaw} field).

OCR datasets

This section presents details of the calculated and measured OCR (OCR_{calc} and OCR_{meas}) datasets, with the Y_{beam} value varied and X_{beam} kept constant, or with the X_{beam} value varied and Y_{beam} kept constant, on the isocenter plane at the reference depth (Z_R) under each irradiation condition. Let the OCR_{calc} components corresponding to the nine dose components mentioned above be expressed as:

$$\mathrm{OCR}_{\mathrm{prim}}^{\mathrm{phan}} = D_{\mathrm{prim}}^{\mathrm{phan}} / D_2^{\mathrm{R}};\ \mathrm{OCR}_{\mathrm{scat}}^{\mathrm{phan}} = D_{\mathrm{scat}}^{\mathrm{phan}} / D_2^{\mathrm{R}};$$
$$\mathrm{OCR}_{\mathrm{prim}}^{\mathrm{wedge}} = D_{\mathrm{prim}}^{\mathrm{wedge}} / D_2^{\mathrm{R}}; \mathrm{OCR}_{\mathrm{scat}}^{\mathrm{wedge}} = D_{\mathrm{scat}}^{\mathrm{wedge}} / D_2^{\mathrm{R}}; \mathrm{OCR}_{\mathrm{prim}}^{\mathrm{w\_hold}} = D_{\mathrm{prim}}^{\mathrm{w\_hold}} / D_2^{\mathrm{R}};$$
$$\mathrm{OCR}_{\mathrm{scat}}^{\mathrm{w\_hold}} = D_{\mathrm{scat}}^{\mathrm{w\_hold}} / D_2^{\mathrm{R}}; \mathrm{OCR}_{\mathrm{prim}}^{\mathrm{MLC}} = D_{\mathrm{prim}}^{\mathrm{MLC}} / D_2^{\mathrm{R}}; \mathrm{OCR}_{\mathrm{scat}}^{\mathrm{MLC}} = D_{\mathrm{scat}}^{\mathrm{MLC}} / D_2^{\mathrm{R}};\ \text{and}\ \mathrm{OCR}_{\mathrm{cont}} = D_{\mathrm{cont}} / D_1^{\mathrm{R}}$$

Then we have:

$$\mathrm{OCR}_{\mathrm{calc}} = \mathrm{OCR}_{\mathrm{prim}}^{\mathrm{phan}} + \mathrm{OCR}_{\mathrm{scat}}^{\mathrm{phan}} + \mathrm{OCR}_{\mathrm{prim}}^{\mathrm{wedge}} + \mathrm{OCR}_{\mathrm{scat}}^{\mathrm{wedge}} + \mathrm{OCR}_{\mathrm{prim}}^{\mathrm{w\_hold}} + \mathrm{OCR}_{\mathrm{scat}}^{\mathrm{w\_hold}} + \mathrm{OCR}_{\mathrm{prim}}^{\mathrm{MLC}} + \mathrm{OCR}_{\mathrm{scat}}^{\mathrm{MLC}} + \mathrm{OCR}_{\mathrm{cont}}. \tag{55}$$

First, we calculated and measured the OCR(X_{beam}, Y_{beam}) datasets, with the Y_{beam} value varied and X_{beam} = 0 cm on the isocenter plane at a reference depth of Z_R = 10 cm, setting

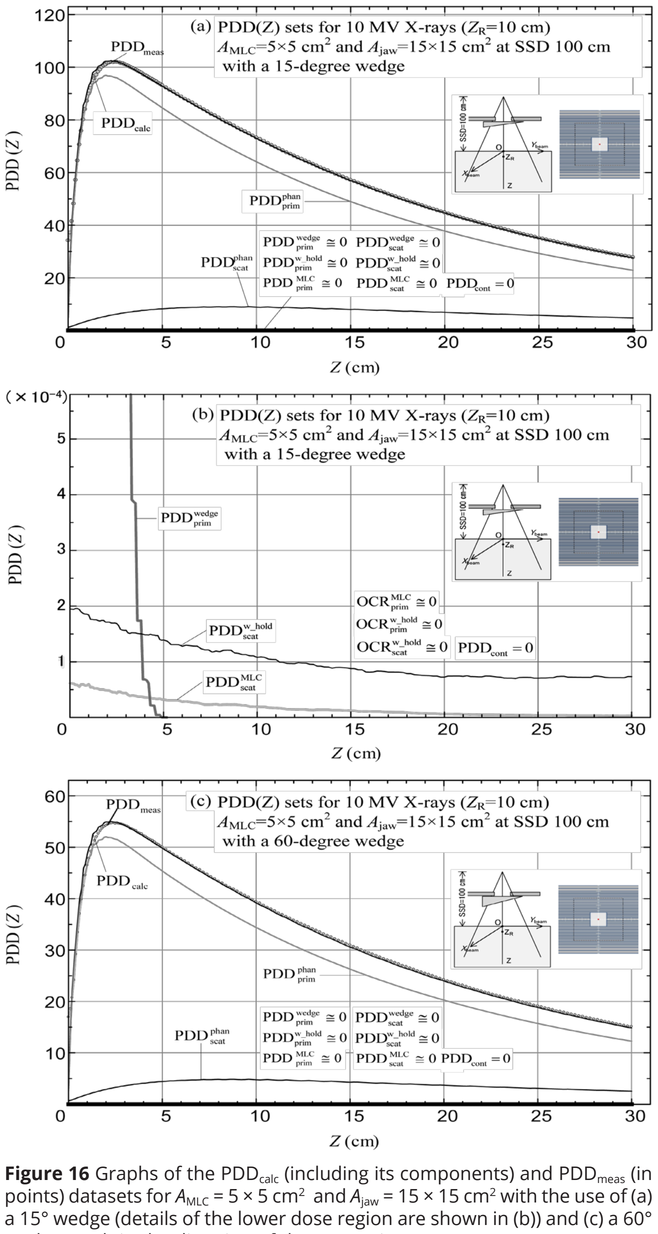

Figure 16 Graphs of the PDD_{calc} (including its components) and PDD_{meas} (in points) datasets for A_{MLC} = 5 × 5 cm² and A_{jaw} = 15 × 15 cm² with the use of (a) a 15° wedge (details of the lower dose region are shown in (b)) and (c) a 60° wedge (each in the direction of the Y_{beam} axis). 10-MV X-rays, SSD = 100 cm (each reference dose was obtained at Z_R = 10 cm using the open A_{jaw} field).

each of the four wedges in the direction of the Y_{beam} axis and with no MLC (A_{MLC} = ∞. When using the 15°, 30° and 45° wedges, we set square jaw fields of A_{jaw} = 5 × 5 - 20 × 20 cm². When using the 60° wedge, we set square jaw fields of A_{jaw} = 5 × 5-15 × 15 cm². Figures 17a-e show the OCR_{calc} (including its components) and OCR_{meas} datasets for a jaw field of A_{jaw} = 15 × 15 cm²: diagram (a) is for the 15° wedge (details of the lower dose components are shown in diagram (b)); diagram (c) is for the 30° wedge; diagram (d) is for the 45° wedge; and diagram (e) is for the 60° wedge. We obtain $\mathrm{OCR}_{\mathrm{scat}}^{\mathrm{w\_hold}} \cong 1\times10^{-5}$ and $\mathrm{OCR}_{\mathrm{scat}}^{\mathrm{wedge}} \cong 5\times10^{-4}$ at points around Y_{beam} = 0 cm. For all the calculation points, we obtain OCR_{cont} = 0, $\mathrm{OCR}_{\mathrm{prim}}^{\mathrm{wedge}} = 0$ and $\mathrm{OCR}_{\mathrm{prim}}^{\mathrm{w\_hold}} = 0$ (because the contaminant electrons and the secondary electrons from the wedge device are all shielded by the wedge and the 10 cm of water). In general, both the OCR_{calc} and OCR_{meas} datasets were in good agreement (with deviations of -0.03 to 0.09% at points around Y_{beam} = 0 cm), except in the case of Figure 17d with a relatively large deviation of -1.5% at points around Y_{beam} = 0 cm (this paper does not analyze further why such large deviations were produced). Results with almost the same calculation accuracy were also obtained for the other OCR datasets.

Next, we calculated and measured the OCR(X_{beam}, Y_{beam}) datasets with the X_{beam} value varied and Y_{beam} = 0 cm on the isocenter plane at each reference depth of Z_R = 2.5, 5 and 10 cm with no wedge used by setting each of the following three MLC leaf-blocked sections within a jaw field of A_{jaw} = 10 × 10 cm². Figures 10a-c show the OCR_{calc} (including its components) and OCR_{meas} datasets for Z_R = 5 cm with the use of MLC leaf-blocked sections: diagram (a) is for one half-leaf (0.5 cm in width); diagram (b) is for three consecutive half-leaves (1.5 cm in width); and diagram (c) is for five consecutive half-leaves (2.5 cm in width). For all the calculation points, we obtained OCR_{cont} ≅ 0 (because the contaminant electrons are practically shielded by the 5-cm-thick water layer), and also obtained $\mathrm{OCR}_{\mathrm{prim}}^{\mathrm{MLC}} \cong 0$ and $\mathrm{OCR}_{\mathrm{scat}}^{\mathrm{MLC}} \cong 0$. It can be seen that the OCR_{meas} data behind the MLC leaf-blocked section by the one half-leaf (Figure 10a) are slightly greater (2.5%) than the OCR_{calc} data because the chamber readings are somewhat influenced by higher doses in the non-leaf-blocked regions, and that, in the non-leaf-blocked regions, the OCR_{calc} data are around 2% greater than the OCR_{meas} data (these large deviations may be due to the assumption that OCR_{source} is a function of only the off-axis distance (R_0); in fact, the basic OCR_{source} dataset was produced based only on in-air dose data measured at points where Y_{beam} ≥ 0 on the Y_{beam} axis). Almost the same calculation accuracy was also observed for the other datasets. It should be emphasized that the work of the $\mathrm{OPF}_{\mathrm{in\_air}}^{\mathrm{multi}}$ factor (equation 47) becomes

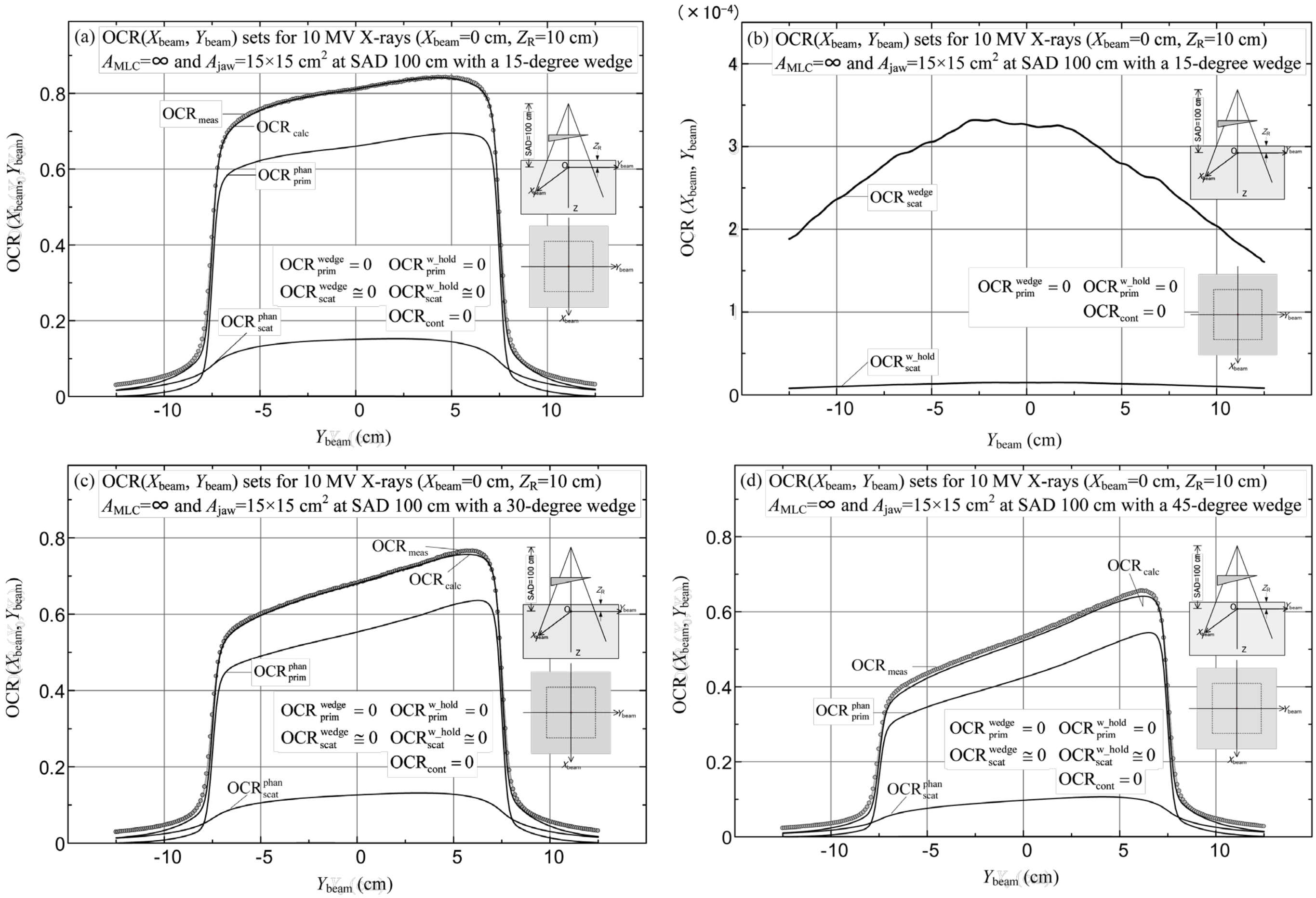

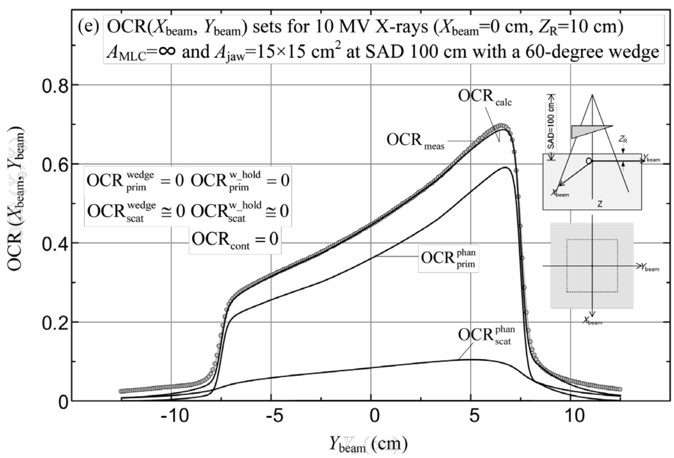

Figure 17 Graphs of the OCR_{calc} (including its components) and OCR_{meas} (in points) datasets, with the Y_{beam} value varied and X_{beam}= 0 cm on the isocenter plane at a reference depth of Z_R = 10 cm , for A_{jaw} = 15 × 15 cm^2 with no MLC and the following wedges set in the direction of the Y_{beam} axis: (a) a 15° wedge (details of the lower dose region are shown in (b)); (c) a 30° wedge; (d) a 45° wedge; and (e) a 60° wedge. 10-MV X-rays, SAD = 100 cm (each reference dose was obtained at Z_R = 10 cm using the open field).

remarkable as the width of an MLC leaf-blocked section in a jaw field becomes narrow. The same statement can also be referred to the cases of Figures 11a-c described in the next place.

Next, we calculated and measured the OCR(X_{beam}, Y_{beam}) datasets with the Y_{beam} value varied and X_{beam} = 1.75 cm on the isocenter plane at each reference depth of Z_R = 2.5, 5 and 10 cm with no wedge used by setting each of the following three MLC leaf-blocked sections in a jaw field of A_{jaw} = 10 × 10 cm^2. Figures 11a-c show the OCR_{calc} (including its components) and OCR_{meas} datasets for X_{beam} = 1.75 cm and Z_R = 10 cm: diagram (a) is for one half-leaf (0.5 cm); diagram (b) is for three consecutive half-leaves (1.5 cm); and diagram (c) is for five consecutive half-leaves (2.5 cm). For all the calculation points, we obtained OCR_{cont} = 0 (because the contaminant electrons are practically all shielded by the 10 cm of water), and also obtained OCR^{MLC}_{prim} =0 and $OCR^{MLC}_{scat}\cong$0. The OCR_{meas} data behind the MLC leaf-blocked section by the one half-leaf (Figure 11a) are slightly greater (3.5%) than the OCR_{calc} data because the chamber readings are also influenced by higher doses in the non-leaf-blocked regions. In Figure 11b, the OCR_{calc} data in the non-leaf-blocked region are around 2% greater than the OCR_{meas} data (this paper does not analyze further why such large deviations were produced). Figure 11a-c reveal that certain amounts of radiation leak at points which are behind the MLC leaf-blocked sections but within the jaw field. Results with almost the same calculation accuracy were also observed for the other datasets.

Next, we calculated and measured the OCR(X_{beam}, Y_{beam}) datasets, with the Y_{beam} value varied and X_{beam} = 0, 1.25 and

3.75 cm on the isocenter plane at each reference depth of Z_R = 2.5, 5 and 10 cm with the use of each of the four wedges in the direction of Y_{beam} axis. For each of the 15°, 30° and 45° wedges, we set an MLC field of A_{MLC} = 5 × 5 cm^2 for the jaw fields of A_{jaw} = 10 × 10, 15 ×15 and 20 × 20 cm^2. For the use of the 60° wedge, we set an MLC field of A_{MLC} = 5 × 5 cm^2 for the jaw fields of A_{jaw} = 10 × 10 and 15 × 15 cm^2. Figures 18a-e show the OCR_{calc} (including its components) and OCR_{meas} datasets for X_{beam} = 0 cm and Z_R = 10 cm with a combination of A_{MLC} = 5 × 5 cm^2 and A_{jaw} = 15 × 15 cm^2 fields: diagram (a) is for the 15° wedge (details of the lower dose region are shown in diagram (b)); diagram (c) is for the 30° wedge; diagram (d) is for the 45° wedge; and diagram (e) is for the 60° wedge. For all the calculation points, we obtained OCR_{cont} = 0, $OCR_{prim}^{MLC}=0$ $OCR_{prim}^{wedge}=0$ and $OCR_{prim}^{w\_hold}=0$ (because the contaminant electrons and the secondary electrons from the MLC and wedge devices cannot reach each of the calculation points), and also obtained $OCR_{scat}^{w\_hold}\cong 0$ and $OCR_{scat}^{MLC}\cong 0$. We obtained OCR_{scat}^{wedge}=3x10^{-5} - 8x10^{-5} at points around Y_{beam} = 0 cm. Figures 18a, c-e show that the deviations of the OCR_{calc} data at Y_{beam} = 0 cm are -0.8%, -1.8%, -1.1% and -1.8%, respectively (these deviations may be caused by the inaccurate estimates of ρ_{wedge_factor} given for the wedges under the given OCR_{source} distribution), and that certain amounts of X-rays leak at points which are outside the MLC field but within the jaw field. Similar results were also observed in other irradiation cases, as described below. Results with almost the same calculation accuracy were also obtained for the other OCR datasets.

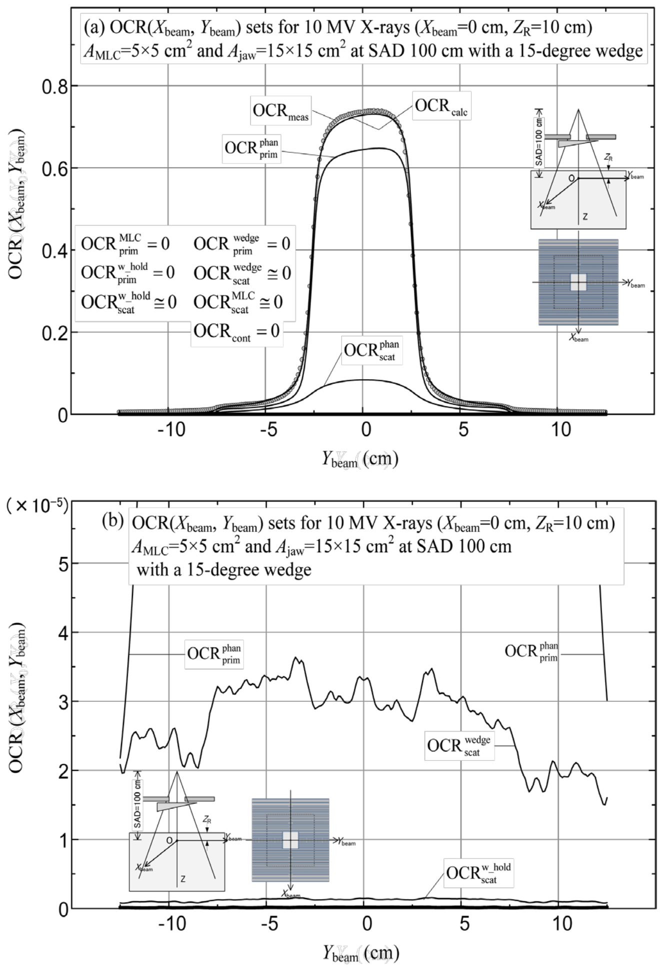

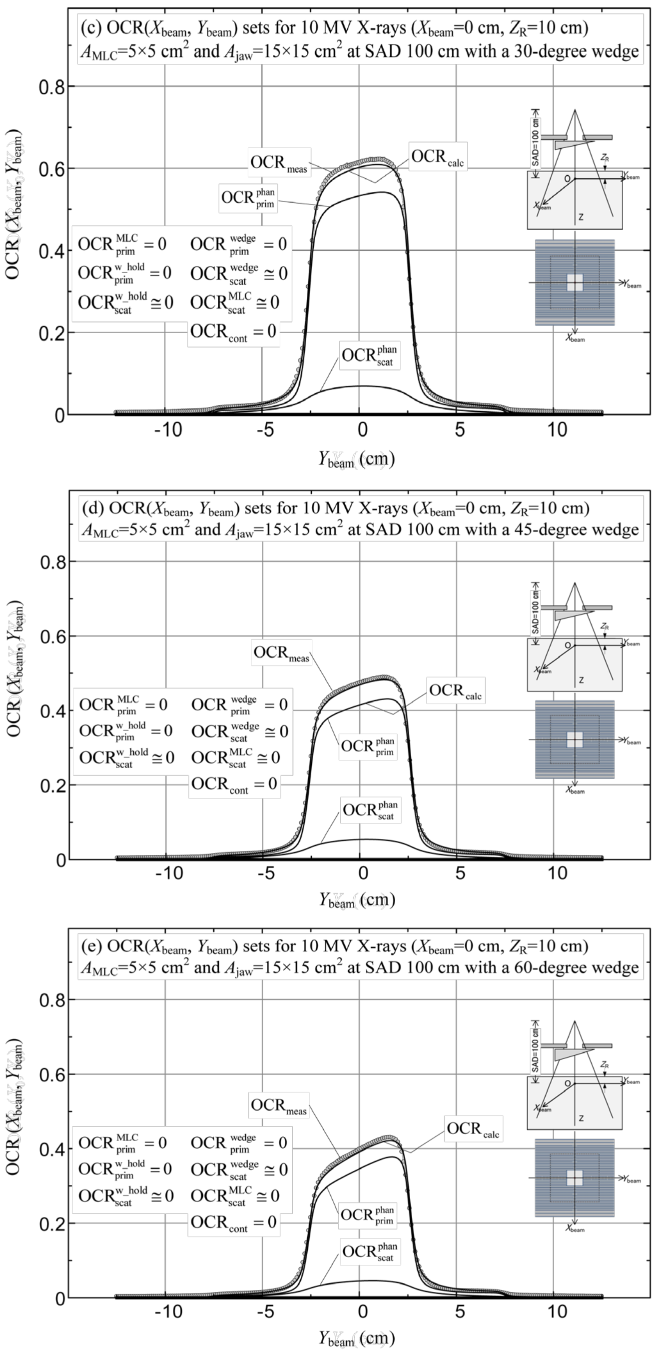

Figure 18 Graphs of the OCR_{calc} (including its components) and OCR_{meas} (in points) datasets, with the Y_{beam} value varied and X_{beam}= 0 cm on the isocenter plane at a reference depth of Z_R = 10 cm, for A_{MLC} = 5 × 5 cm^2 and A_{jaw} = 15 × 15 cm^2 with the use of (a) a 15° wedge, (b) details of the lower dose region, (c) a 30° wedge, (d) a 45° wedge and (e) a 60° wedge (each in the direction of the Y_{beam} axis). 10-MV X-rays, SAD=100 cm (each reference dose was obtained at Z_R = 10 cm using the open A_{jaw} field).

Next, we calculated and measured the OCR(X_{beam}, Y_{beam}) datasets, with the Y_{beam} value varied and X_{beam} = 0, 1.25 and 3.75 cm on the isocenter plane at each reference depth of Z_R = 2.5, 5 and 10 cm using each of the four wedges in the direction of the Y_{beam} axis. When using the 15°, 30° and 45° wedges, we set square jaw fields of A_{jaw} = 5 × 5 - 20 × 20 cm^2 When using the 60° wedge, we set square jaw fields of A_{jaw} = 5 × 5 - 15 × 15 cm^2. Figures 19a-c show the OCR_{calc} (including its components) and OCR_{meas} datasets for 10 cm, with the use of the 45° wedge for a combination of A_{MLC} = 5 × 5 cm^2 and A_{jaw} = 15 × 15 cm^2 fields: diagram (a) is for X_{beam} = 0 cm; diagram (b) is for X_{beam} = 1.25 cm; and diagram

(c) is for X_{beam} = 3.75 cm. For all the calculation points, we obtained OCR_{cont} = 0 (because the contaminant electrons are all shielded by the wedge and the 10 cm thick water layer), and also obtained OCR_{prim}^{wedge}=0, $OCR_{prim}^{w\_hold}$ =0 and OCR_{prim}^{MLC}=0 (because the secondary electrons from the MLC and wedge devices cannot reach each of the calculation points). We obtained OCR_{scat}^{wedge}=7x10^{-5}, $OCR_{scat}^{w\_hold}$≅0 and OCR_{scat}^{MLC}≅0 at points around Y_{beam} = 0 cm. The OCR_{calc} deviations at Y_{beam} = 0 cm are -1.1% in Figure 19a -1.9% in Figure 19b (these deviations may also be caused by the inaccurate estimate of ρ_{wedge_factor} given for the wedge under the given OCR_{source} distribution). Figure 19c similarly shows the results for X_{beam} = 3.75 cm outside the A_{MLC} field, illustrating the sharp changes in dose distribution near the point of Y_{beam} = 0 cm (due to the large X-ray leakage from the closed parts, where the pairs of A- and B-MLC leaves are just closed). It also demonstrates that the OCR_{meas} data are smaller than the OCR_{calc} data at points around Y_{beam} = 0 cm, because the measurements by the chamber reflect the lower doses in the MLC-shielded region. Figure 19a-c show that certain amounts of X-rays leak at points which are outside the MLC field but within the jaw field. Almost the same calculation accuracy was also observed for the other OCR datasets.

Finally, we calculated and measured the OCR(X_{beam}, Y_{beam}) datasets, with the X_{beam} value varied and Y_{beam} = 0, -1.25 and -3.75 cm on the isocenter plane at each reference depth of Z_R = 2.5, 5 and 10 cm, using the four wedges in the direction of the X_{beam} axis. When using the 15°, 30° and 45° wedges, we set square jaw fields of A_{jaw} = 5 × 5 - 20 × 20 cm^2 for an MLC field of A_{MLC} = 5 × 5 cm^2. When using the 60° wedge, we set square jaw fields of A_{jaw} = 5 × 5 - 15 × 15 cm^2 for an MLC field of A_{MLC} = 5 × 5 cm^2. Figures 20a-c show the OCR_{calc} (including its components) and OCR_{meas} datasets for Z_R = 10 cm with the use of the 45° wedge for a combination of A_{MLC} = 5 × 5 cm^2 and A_{jaw} = 15 × 15 cm^2 fields: diagram (a) is for Y_{beam} = 0 cm; diagram (b) is for Y_{beam} = -1.25 cm; and diagram (c) is for Y_{beam} = -3.75 cm. These OCR_{calc} and OCR_{meas} results clearly indicate variations in X-ray beam attenuation along the direction of wedge insertion. With respect to each of the diagrams, we obtained OCR_{cont} = 0, OCR_{prim}^{MLC}=0, OCR_{prim}^{wedge} =0 and $OCR_{prim}^{w\_hold}$=0 for all the calculation points (because the contaminant electrons and the secondary electrons from the MLC and wedge devices cannot reach each of the calculation points); and we obtained OCR_{scat}^{wedge}≅7.5x10^{-5}, $OCR_{scat}^{w\_hold}$≅0 and OCR_{scat}^{MLC}≅0 , near the point of X_{beam} = 0 cm Figure 20a shows waveform dose distributions in the left- and right-hand regions that are outside the MLC field but within the jaw field, where the pairs of A- and B-MLC leaves are just closed. In the waveform dose distributions, the OCR_{meas} data are much smaller than the OCR_{calc} data because the measurements by the chamber of finite size reflect the lower doses in the MLC-shielded region. There are relatively large deviations in OCR_{calc} resulting from the measurement (OCR_{meas}) at X_{beam} = 0 cm; Figure 20a shows -1.1%, and Figure 20b shows -1.7% (these deviations may also be caused by the inaccurate magnitude of ρ_{wedge_factor} given for the wedge under the given OCR_{source} distribution). Figure 20c shows the OCR datasets outside the A_{MLC} field, illustrating waveform dose distributions outside the A_{MLC} field but within the jaw field, with pairs of large and small

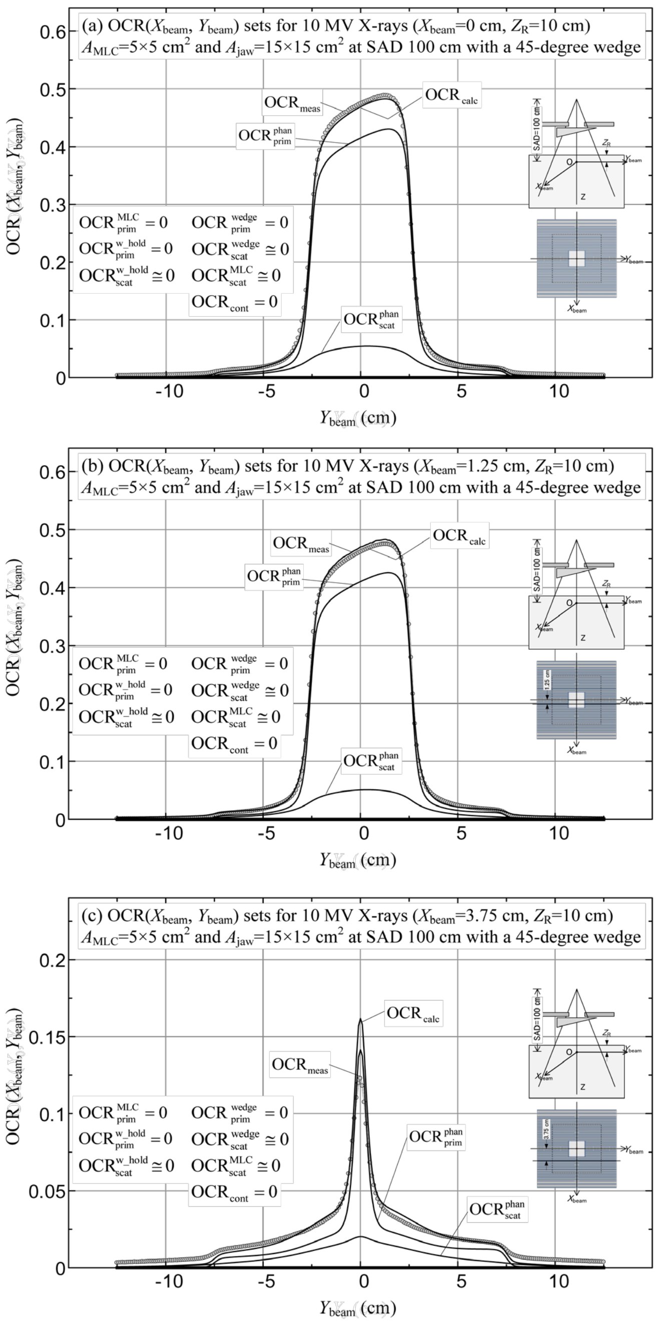

Figure 19 Graphs of OCR_{calc} (including its components) and OCR_{meas} (in points) datasets, with the Y_{beam} value varied and (a) X_{beam} = 0 cm (b) X_{beam} = 1.25 cm and (c) X_{beam} = 3.75 cm on the isocenter plane at a reference depth of Z_R = 10 cm, with the use of a 45° wedge in the direction of the Y_{beam} axis for A_{MLC} = 5 × 5 cm^2 and A_{jaw} = 15 × 15 cm^2. 10-MV X-rays, SAD = 100 cm (each reference dose was obtained at Z_R =10 cm using the open A_{jaw} field).

waves repeated (reflecting the geometrical features of the half leaves of types 1 and 2 as shown in Figures 12 and 13, and clearly showing X-ray leakages in the corresponding region). Almost the same calculation accuracy was also observed for the other OCR datasets.

Figures 21a-d show the OCR_{calc} (including its components) and OCR_{meas} datasets for Z_R = 2.5 cm with the use of the 60° wedge for a combination of A_{MLC} = 5 × 5 cm^2 and A_{jaw} = 15 × 15 cm^2 fields: diagram (a) is for Y_{beam} = 0 cm (details of the lower dose region are shown in diagram (b)); diagram (c) is for Y_{beam} = -1.25 cm; and diagram (d) is for Y_{beam} = -3.75 cm. Almost the same calculation accuracy was also observed for the other OCR datasets. It should be noted that the dose leakage characteristics of the MLC are almost the same as those obtained by using a Monte Carlo simulation model [25] (Figures 20a, c and Figures 21a, d).

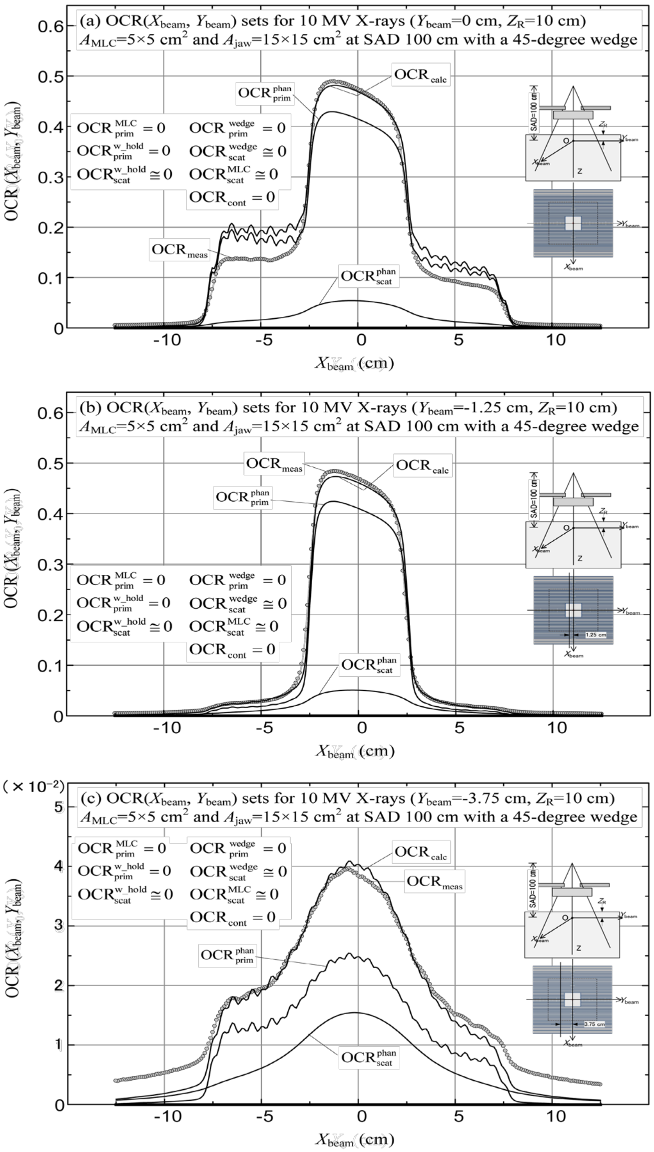

Figure 20 Graphs of OCR_{calc} (including its components) and OCR_{meas} (in points) data, with the X_{beam} value varied and (a) Y_{beam} = 0 cm (b) Y_{beam} = -1.25 cm and (c) Y_{beam} = -3.75 cm on the isocenter plane at a reference depth of Z_R = 10 cm, with the use of a 45° wedge in the direction of X_{beam} axis for A_{MLC} = 5 × 5 cm^2 and A_{jaw} = 15 × 15 cm^2 10-MV X-rays, SAD = 100 cm (each reference dose was obtained at Z_R = 10 cm using the open A_{jaw} field).

As the above-described PDD and OCR datasets show, the OCR datasets can, in general, reflect levels of dose calculation accuracy to a greater extent than the PDD datasets can. One of the most basic functions for a given linear accelerator is the OCR_{source} function, defined in an open infinite A_{jaw} field (equation 23). As the OCR_{source} function used in this study shows, it may not be reasonable to assume that the OCR_{source} function is determined only by the off-axis distance $\left(R_0=\sqrt{X_0^{\,2}+Y_0^{\,2}}\right)$ on the isocenter plane; instead, it should generally be determined by the 2D position of (X_0, Y_0). Moreover, the magnitude of ρ_{wedge_factor} for each wedge should be determined after acquisition of an accurate OCR_{source} dataset.

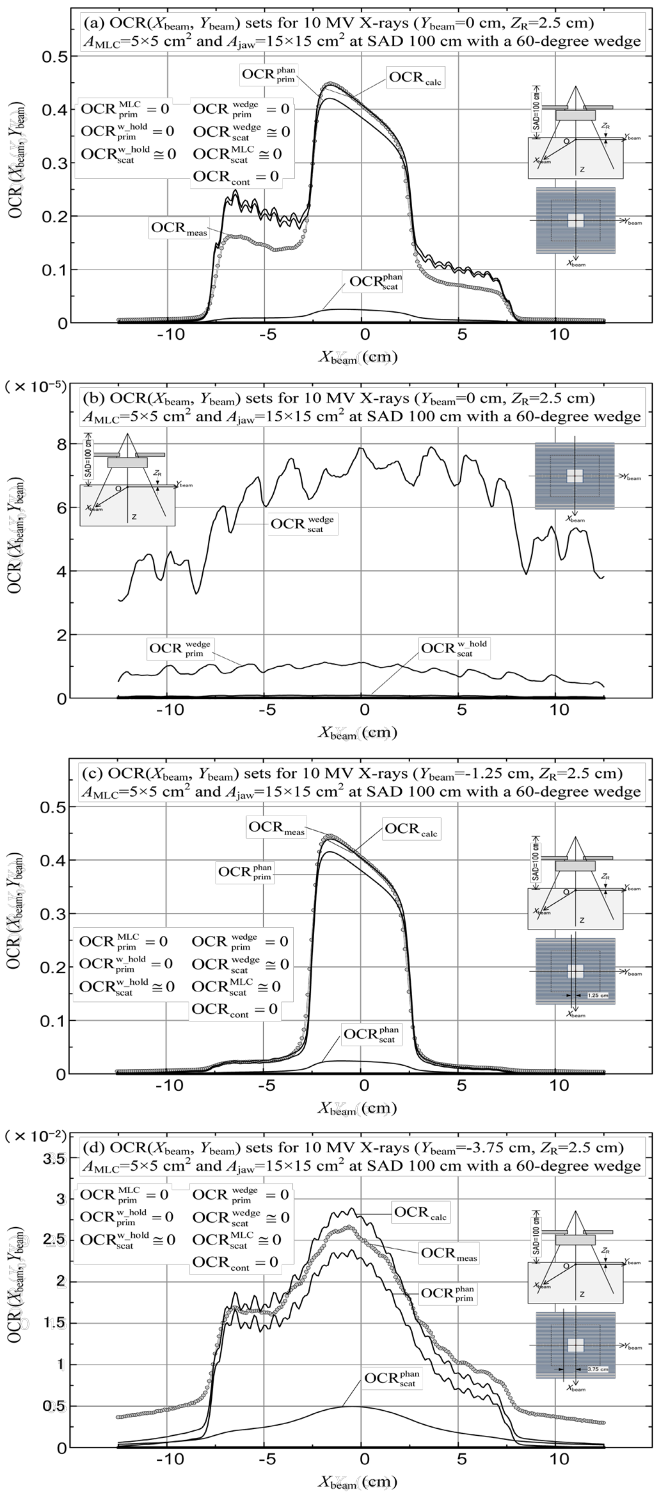

Figure 21 Graphs of OCR_{calc} (including its components) and OCR_{meas} (in points) datasets, with the X_{beam} value varied and (a) Y_{beam} = 0 cm (details of the lower dose region are shown in (b)), (c) Y_{beam} = -1.25 cm and (d) Y_{beam} = -3.75 cm on the isocenter plane at a reference depth of Z_R = 2.5 cm with the use of a 60° wedge in the direction of the X_{beam} axis for A_{MLC} = 5 × 5 cm^2 and A_{jaw} = 15 × 15 cm^2. 10-MV X-rays, SAD=100 cm (each reference dose was obtained at Z_R = 2.5 cm using the open A_{jaw} field).

We performed theoretical and experimental studies on 10-MV X-ray dose calculations in water phantoms with multileaf collimation (MLC) and/or wedge filtration using a linear accelerator equipped with (in order from the source side) a pair of upper jaws, a pair of lower jaws, an MLC and a wedge filter. The dose calculation simulations were performed, focusing on percentage depth dose (PDD) and off-center ratio (OCR) datasets.

The dose calculations were based on a convolution method using primary and scatter dose kernels formed for energy bins of X-ray spectra reconstructed as a function of the off-axis distance. We used the MLC leaf-field output subtraction method to calculate the in-air beam intensity for points on the isocenter plane for an open MLC field under a given jaw field, employing a small, extended radiation source on the X-ray target and a large, extended radiation source on the flattening filter. The in-air beam intensity was then decomposed into each energy-bin component (E_N) of the reconstructed X-ray spectra.

The 3D structures of the jaw collimator, MLC and wedge devices were replaced with 2D plates for simple dose calculation. The in-phantom dose calculation was performed by treating the phantom, the wedge, and the MLC as parts of a unified irradiated body, where we proposed to use a factor of $\mu_{\mathrm{med}}(E_N) / \mu_{\mathrm{water}}(E_N)$ (the relative attenuation factor) for each energy-bin component (E_N), instead of the relative electron density (ρ_e), for the medium of each volume element within the unified irradiated body, where $\mu_{\mathrm{med}}(E_N)$ and $\mu_{\mathrm{water}}(E_N)$ are the linear attenuation coefficients for E_N photons of the volume element material and water.

Conclusions

It is confirmed that, as the MLC leaf-blocked section width became narrow, the in-phantom dose calculation effect due to nonuniform incident beam intensities became great. A correction factor was then introduced for each ΔV element in the phantom. The in-phantom dose was generally separated into nine dose components: (a) the primary and scatter dose components produced in the phantom, (b) the primary and scatter dose components emanating from the MLC, (c) the primary and scatter dose components emanating from the wedge body, (d) the primary and scatter dose components emanating from the wedge holder, and (e) the contamination dose component caused by the electrons emanating from the treatment head and the air volume.

Acknowledgments

The authors are grateful to Mr. H. Mikami for his helpful advice and timely guidance throughout this study. Part of this work was performed by Yoshihisa Niioka, Takahito Chiba and Keita Masaki for their graduate studies at the Hirosaki University Graduate School of Health Sciences.

Conflicts of interest

This study was carried out in collaboration with Technology of Radiotherapy Corporation, Tokyo, Japan. This sponsor had no control over the interpretation, writing, or publication of this work.

Supplementary data

Supplementary data associated with this article can be found, at http://nobleresearch.org/doi/10.14312/2399-8172.2017-2. These data include appendix- A, B, C, and D.

References

[1] Ahnesjö A, Aspradakis MM. Dose calculations for external photon beams in radiotherapy. Phys Med Biol. 1999; 44(11):R99–155.

[2] Ahnesjö A. Collapsed cone convolution of radiant energy for photon dose calculation in heterogeneous media. Med Phys. 1989; 16(4):577–592.

[3] Iwasaki A, Kubota M, Hirota J, Fujimori A, Suzaki K, et al. Characteristic features of a high-energy X-ray spectra estimation method based on the Waggener iterative perturbation principle. Med Phys. 2006; 33(11):4056–4063.

[4] Iwasaki A, Kimura S, Sutoh K, Kamimura K, Sasamori M, et al. Reconsideration of the Iwasaki–Waggener iterative perturbation method for reconstructing high-energy X-ray spectra. Radiol Phys Technol. 2012; 5(2):248−269.

[5] Iwasaki A. Comments on the primary and scatter dose-spread kernels used for convolution methods. Radiat Phys Chem. 2002; 65(6):595−597.

[6] Iwasaki A, Kimura S, Sutoh K, Kamimura K, Sasamori M, et al. A convolution/superposition method using primary and scatter dose kernels formed for energy bins of X-ray spectra reconstructed as a function of off-axis distance: a theoretical study on 10-MV X-ray dose calculations in thorax-like phantoms. Radiol Phys Technol. 2011; 4(2):203−215.

[7] Kimura S, Sutoh K, Kamimura K, Iwasaki A, Sasamori M, et al. A convolution/superposition method using primary and scatter dose kernels formed for energy bins of X-ray spectra reconstructed as a function of off-axis distance: Comparison of calculated and measured 10-MV X-ray doses in thorax-like phantoms. Radiol Phys Technol. 2011; 4(2):216−224.

[8] Hubbell JH. Photon mass attenuation and energy-absorption coefficients. Int J Appl Radiat Isot. 1982; 33(11):1269−1290.

[9] O'Connor JE. The variation of scattered X-rays with density in an irradiated body. Phys Med Biol. 1957; 1(4):352–369.

[10] Woo MK, Cunningham JR. The validity of the density scaling method in primary electron transport for photon and electron beams. Med Phys. 1990; 17(2):187–194.

[11] Iwasaki A, Ishito T. The differential scatter-air ratio and differential backscatter factor method combined with the density scaling theorem. Med Phys. 1984; 11(6):755–763.

[12] Miyashita H, Hatanaka S, Fujita Y, Hashimoto S, Myojyoyama A, et al. Quantitative analysis of in-air output ratio. J Radiat Res. 2013; 54(3):553–560.

[13] Medina AL, Teijeiro A, Garcia J, Esperon J, Terron JA, et al. Characterization of electron contamination in megavoltage photon beams. Med Phys. 2005; 32(5):1281–1292.

[14] Asuni G, Jensen JM, McCurdy BMC. A Monte Carlo investigation of contaminant electrons due to a novel *in vivo* transmission detector. Phys Med Biol. 2011; 56(4):1207−1223.

[15] González W, Anguiano M, Lallena AM. A source model for the electron contamination of clinical linac heads in photon mode. Biomed Phys Eng Express. 2015; 1(2):025202.

[16] Kimura S, Iwasaki A, Sutoh K, Seino M, Komai F, et al. Calculation of MLC in-air outputs using a leaf-field output subtraction method. Proc. of the 15th Int. Conf. on the Use of Computers in Radiation Therapy. 2007; 1:425−429.

[17] Zhu TC, Bjärngard BE. Head scatter off-axis for megavoltage X-rays. Med Phys. 2003; 30(4):533−543.

[18] Zhu TC, Bjärngard BE, Xiao Y, Yang CJ. Modeling the output ratio in air for megavoltage photon beams. Med Phys. 2001; 28(6):925−937.

[19] Zhu TC, Bjärngard BE, Xiao Y, Bieda M. Output ratio in air for MLC shaped irregular fields. Med Phys. 2004; 31(9):2480−2490.

[20] Zhu TC, Ahnesjö A, Lam KL, Li XA, Ma C-MC, et al. Report of AAPM Therapy Physics Committee Task Group 74: In-air output ratio, S_c, for megavoltage photon beams. Med Phys. 2009; 36(11):5261−5291.

[21] Khan FM, Sewchand W, Lee J, Williamson JF. Revision of tissue-maximum ratio and scatter-maximum ratio concepts for cobalt 60 and higher energy X-ray beams. Med Phys. 1980; 7(3):230−237.

[22] Khan FM. The physics of radiation therapy; 3rd edition. 2003.

[23] Boyer A, Biggs P, Galvin J, Klein E, LoSasso T, et al. Basic applications of multileaf collimators: Report of the AAPM Radiation Therapy Committee Task Group No. 50: AAPM Report No. 72 ed. Madison, USA: Medical Physics Publishing. 2001.

[24] van Gasteren JJM, Heukelom S, van Kleffens HJ, van der Laarse R, Venselaar JLM, et al. The determination of phantom and collimator scatter components of the output of megavoltage photon beams: Measurement of the collimator scatter part with a beam-coaxial narrow cylindrical phantom. Radiother Oncol. 1991; 20(4):250−257.

[25] Heath E, Seuntjens J. Development and validation of a BEAMnrc component module for accurate Monte Carlo modelling of the Varian dynamic Millennium multileaf collimator. Phys Med Biol. 2003; 48(24):4045−4063.